Experimental study of steady and transient subcooled flow boiling

V. Scheiff[a,b], F. Bergame[b], J. Sebilleau[b], P. Ruyer[a], C. Colin[b,*]

[a] Institut de Radioprotection et de Sûreté Nucléaire (IRSN), PSN-RES/SEMIA/LSMA, BP3, St Paul-Lez-Durance, 13115, France
[b] Institut de Mécanique des Fluides de Toulouse, Université de Toulouse, CNRS, Allée Camille Soula, Toulouse, 31400, France

ARTICLE INFO

Keywords:
Nucleate flow boiling
Transient heating
Wall heat flux
Bubble dynamics
Infrared thermography

ABSTRACT

This study aims to better characterize the heat transfer and flow structure in the fully developed nucleate flow boiling regime in a semi-annular duct. Experiments with a refrigerant HFE7000 were performed in the range of Reynolds numbers from 13 000 to 40 500, subcoolings close to 15 °C, for constant heating power, constant wall temperature and constant heating rates (linear increase of the wall temperature).

With constant heating power, the wall heat flux is well predicted by a Chen-type correlation based on a contribution due to the forced convection and a contribution due to nucleate boiling, including the effect of the liquid subcooling. A thin layer of bubbles sliding along the wall is observed. The characteristic diameter of the bubbles increases with the heat flux and decreases with the liquid velocity and its subcooling. The bubble diameters can be well predicted versus 3 dimensionless numbers: the Reynolds number of the flow, the Jakob number based on the liquid subcooling and the Boiling number. A drag coefficient of the bubbles sliding on the wall is estimated from the measurements of the bubble relative velocities and is in good agreement with the recent numerical simulation of Shi et al. [1] for a spherical bubble moving close to a wall in a shear flow. In the experiments with a constant set temperature, a non-homogeneity of the surface temperatures is observed as well as high fluctuations of temperatures and heat fluxes. The heat transfer is strongly degraded ($\simeq$ 60%) by comparison with heating with a set power. Finally a transient nucleate boiling regime with a constant temperature increase dT/dt is investigated. For $dT/dt < 50$ °C.s^{-1}, the results are similar to those of Auracher and Marquardt and a correlation for the prediction of the wall heat flux versus the wall temperature in the transient nucleate boiling regime is provided.

1. Introduction

Nucleate boiling is known as an efficient heat transfer regime, thanks to a combination of bubbly induced convection and latent heat transport. In steady conditions, heat flux from the wall to the fluid is fully determined, for a given set of fluid and wall properties and geometries, by the liquid bulk temperature, the liquid flow rate and the wall superheat. In this study, we consider the impact of transient heating of the wall on the nucleate boiling heat transfer, i.e.: how a fast variation of these control parameters affects the boiling heat transfer. From a phenomenological point of view, when the wall temperature varies over time scales smaller than the typical boiling process (e.g. the bubble life cycle on the wall, from nucleation to departure), the heat transfer is expected to be impacted by the wall heating rate.

Auracher and Marquardt [2] studied the transient heat transfer in pool boiling with rates of wall temperature increase up to 40 K.s^{-1}. Sakurai and Shiotsu [3] more extensively studied transient boiling up to critical heat flux on immersed wires for exponentially increasing power transients, identifying specific spontaneous heterogeneous nucleation phenomena for very rapid heating, which were also observed by Fau et al. [4]. For rather similar conditions, Su et al. [5] have considered convective boiling over a plate. In less academical configurations, related to the study of hypothetical accidental power transient in the reactor vessel of a nuclear power plant (so called reactivity initiated accident scenario), a large deviation of the heat transfer coefficient with respect to corresponding steady conditions has also been reported [6,7]. The authors pointed out that the boiling crisis is not due to hydrodynamic instabilities, as it is proposed by the classical correlations of the literature, but to the coalescence of vapour bubbles on the rod surface: relatively low power transients lead to the establishment of the steady nucleate boiling regime while high power transients lead to the boiling crisis, namely to the formation of a vapor blanket and the establishment of film boiling. They conclude that

* Corresponding author.
E-mail addresses: catherine.colin@imft.fr, colin@imft.fr (C. Colin).

https://doi.org/10.1016/j.ijheatmasstransfer.2020.120548

Nomenclature

Bo	Boiling number, $Bo = \frac{\Phi_{gen}}{h_{lv}.G}$
Re	Reynolds number, $Re = \frac{GD_h}{\mu_l}$
S	Surface section (m^2)
$\mathcal{U}$	Voltage (V)
$\mathcal{I}$	Current (A)
$\mathcal{P}$	Generated power, $\mathcal{P} = \mathcal{U}\mathcal{I}$, (W)
e	Thickness (m)
C_p	Specific heat capacity ($J.kg^{-1}.K^{-1}$)
t	Time (s)
T	Temperature (K)
L_c	Capillary length (m)
Ja	Jakob number $Ja = \frac{\rho_l C_{p,l} \Delta T}{\rho_v h_{lv}}$
La	Laplace number $La = \frac{\rho_l L_c \sigma}{\mu^2}$
h_{lv}	Latent heat of vaporisation ($J.kg^{-1}$)
D_b	Bubble size (m)
D_h	Hydraulic diameter (m)
F_D	Drag force (N)
C_D	Drag Coefficient
V	Speed ($m.s^{-1}$)
g	Gravity ($m.s^{-2}$)
R	Resistance (Ω)
R	Height (m)
M_{th}	Thermal Mass ($J.m^{-2}.K^{-1}$)
a	Electrical resistivity coefficient
G	Mass flux ($kg.m^{-2}.s^{-1}$)
ρ	Density ($kg.m^{-3}$)
τ	Characteristic time (s)
ϕ	Heat flux ($W.m^{-2}$)
σ	Surface tension ($N.m^{-1}$)
w	Wall
exp	Experimental
th	Theoretical
l	Liquid
gen	Generated by Joule effect
v	Vapour
p	Paint
sat	Saturation
set	Setpoint
sub	Subcooled

a more detailed analysis of the physical mechanisms is needed to provide a reliable modeling of the heat transfer on the nuclear fuel rod during a reactive initiated accident.

In order to better analyse and understand the physical mechanisms encountered in transient boiling regimes, a dedicated experimental facility has been built by Visentini et al. [8]. It allows generating various power transients within a wall in contact with a subcooled turbulent liquid flow of HFE700 with a maximal Reynolds number value of 60 000. Thanks to an infrared camera and a high-speed camera, it is possible to evaluate the heat flux transferred to the liquid and study all the regimes from the convection (Baudin et al. [9]) to the film boiling while relating the time evolution of the heat transfer with the development of two-phase flow structures along the wall. Onset of nucleate boiling has been already studied in details in a companion paper [10].

In recent studies (Golobič and Zupančič [11], Petkovsek et al. [12], Richenderfer et al. [13]) the authors use new metrology (high-speed infrared thermography) that allow to access the wall temperature field and to determine its correlation with the bubble nucleation and growth processes. Coupled with a high-speed camera, the infrared camera allows to accurately measure the wall temperature, estimate the wall-to-fluid heat transfer and characterize the boiling flow topology in the Fully Developed Nucleate Boiling regime and in particular how the bubbly layer thickness is related to heat transfer. The main goal of the present study is therefore to characterize the nucleate boiling process in convective subcooled conditions both in steady and transient conditions. It is difficult to control nucleate boiling experiments with imposed transient power conditions. Indeed, for rapid power increase, transient nucleate boiling lasts a very short time (before boiling crisis): the power supply is cut off during the test to avoid a burnout of the test section. Using a Proportional Integrator Derivator (P.I.D.) system to control transient power by setting a constant wall temperature increase rate, allows to study more extensively transient nucleate boiling regime up to 500 $K.s^{-1}$.

Table 1
Test conditions.

Generic symbol	Test section #	Test conditions		
		Re = 13 500	27 000	40 500
○	SE_1	Ja_{sub} = 21.5	Ja_{sub} = 20	Ja_{sub} = 20.8
□	SE_2	Ja_{sub}=22	⌀	⌀
♦	SE_2	Ja_{sub}=27	Ja_{sub}=26	⌀
✚	SE_3	Ja_{sub}=23	⌀	⌀
–♦–	SE_4	Ja_{sub}=22	⌀	⌀

The paper is organized as follows. First, in Section 2, we present the experimental device and its instrumentation. Heat transfer and related bubbly layer characteristics are analyzed in Section 3 for steady conditions. Transient nucleate boiling is then studied in Section 4.

2. Description of the experimental set-up

The experimental set-up used for this study has been detailed in the previous works of Visentini et al. [8] and Scheiff et al. [10]. The main part of the cell consists of a subcooled flow of a refrigerant, HFE7000, in a semi annular section composed of a thin metal foil of thickness e_w = 50 µm and radius 4.1 mm rapidly heated by Joule effect. The fluid is confined in the semi-annular gap between the metal foil and an outer glass cylinder of radius 17 mm as illustrated in Fig. 1. The test cell is inserted in a flow loop consisting of a gear pump, a Coriolis flow meter, a preheater to fix the liquid temperature ($T_l \in$ [15; 25] °C.), a 1 m long channel upstream the test section to establish the flow, and a condenser. The experiments are carried out at a constant liquid flow rate (corresponding to Reynolds numbers between 0 and 60,000). The velocity field in single-phase flow has been carefully measured by P.I.V. in the symmetry plane and computed in the cross section by using StarCCM+ [9]. The mean axial velocity in the symmetry plane is in good agreement with the analytical expression of Kaneda et al. [14] for an annular geometry. The electrical power is applied between the two ends of the metal foil (Gen+, Gen- in Fig. 1). It is provided by a power supply SORENSEN SGA with 0–40 V voltage range and 0–250 A current range.

Boiling crisis occurrence leads to partial burnout of the foil and it is then required to rebuild the test section. Even using the same metal, the foil properties differ between different test sections in terms of position and the size of the nucleation sites. The experimental results presented are obtained for three different test sections named SE_1, SE_2 and SE_3 for power control but a single test section SE_4 for temperature control. The experimental conditions are given in Table 1.

Flow rates correspond to different colors. red: 0.1 $l.s^{-1}$, blue: 0.2 $l.s^{-1}$, green: 0.3 $l.s^{-1}$. Liquid bulk temperature are represented by different symbols. The subcooling of the inlet liquid flow $\Delta T = T_{sat}$ - T_l is here indicated in terms of $Ja_{sub} = \frac{\rho_l C_{p,l} \Delta T}{\rho_v h_{lv}}$ varying from

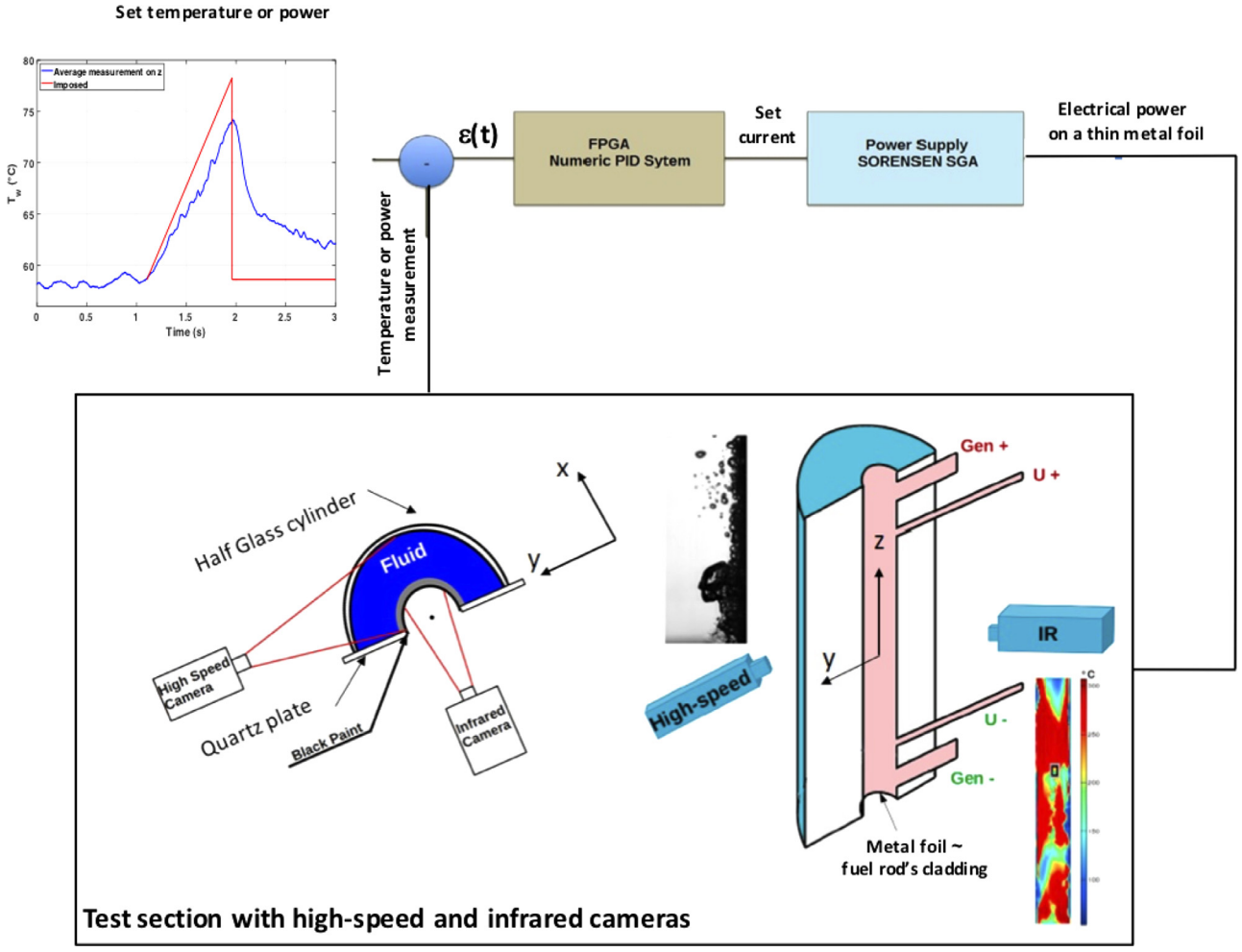

Fig. 1. Test section with high-speed and infrared images.

$\Delta T = 13$ °C for Ja_{sub}=20 to $\Delta T = 17$ °C for Ja_{sub}=27. Finally, the generated heat flux, Φ_{gen} is imposed between 40 and 80 kW.m^{-2}.

Note that in the experiments, the mean liquid temperature increase along the heated test section is less than 1 °C for the highest heat flux and the lower liquid flow rate. Therefore, the liquid subcooling (namely the Ja_{sub} value) measured at the inlet of the test section can be considered as representative of the local subcooling all along the test section.

2.1. Measurements techniques and image processing

Two perpendicular cameras are used during the tests (Fig. 1). An infrared camera CEDIP JADE III placed behind the foil provides a temperature field of the heated foil's back surface. The camera has a [3.5-5.1] µm sensitivity range and a focal plane array detector of 240x320 px^2 cooled by a Stirling MCT. For this study, the acquisition frequency is 500 fps and the view field is 20x120 px^2. 1 pixel corresponds to 470 µm and the whole picture covers a 5 cm long portion of the metal foil filmed along the flow direction. The integration time ranges between 20 and 500 μs. The infrared camera is calibrated thanks to a DCN 1000 N4 black body. The uncertainties on the measurement temperature of the black surface depend on the temperature range of calibration. Over the [20 °C-100 °C] temperature range of our experiments, the uncertainty varies from ± 0.6 °C at 20 °C to ± 0.1 °C at 100 °C.

To increase temperature measurements accuracy, the backside of the metal foil is covered with a layer (e_p ~ 35 ± 5 µm thickness) of black paint with large emissivity (0.94). The black paint used is a Belton Spectral RAL 9005 MAT BLACK paint, which thermal properties were measured by the company NeoTIM (Albi, France), and are given in Table B1. The thickness of the paint has been chosen as a best compromise between getting the largest surface emissivity and sufficiently low thermal inertia. Solving a 1D conduction through the metal foil and the paint layer, showed that the thermal gradient between the paint and the metal foil is negligible (Scheiff et al. [10]). Since the surface is curved, its emissivity depends on the observation angle. Only a width of 5 pixels (2.35mm) on both sides of the symmetry plane is taken into account in the measurement of the surface temperature. A high-speed camera focuses on a lateral view of the two-phase flow along the test section (see Fig. 1). The high-speed camera image size is 384x1024 px^2 where 1 pixel corresponds to 80 µm. So these high-speed camera images allow a resolution of approximately 10 px for each individual bubble (given the typical bubble size observed during our experiments). Those images are used to focus on the bubbly layer just over the wall. Using Matlab software, after binarizing the images and removing bubbles not in contact with the wall, the following quantities are determined over this bubbly layer: time evolution of its thickness, bubble axial velocities, percentage of surface wetted by the liquid.

It is not the case for the infrared camera with a lower spatial resolution. It is not possible to identify nucleation sites from thermal analysis. Both cameras provide complementary information during tests that are useful for the interpretation of the re-

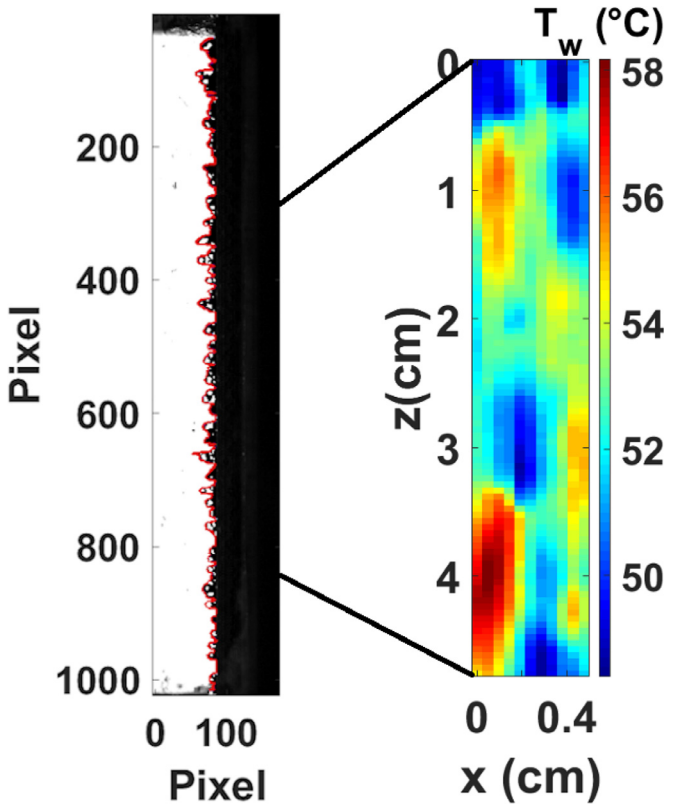

Fig. 2. Raw and processed images obtained with the high speed camera, coupling with the infrared camera on the same zone at the same time.

sults. Visualizations of the two cameras have been synchronized in space and time (Fig. 2). An integrated trigger connected to the NI box allows synchronizing videos with data from other measurement channels.

2.2. Heating control

The experimental set-up allows the study of steady and transient nucleate boiling regimes. For the transient boiling phenomena study, either the power or the temperature can be controlled thanks to a P.I.D. feedback control system based on a Labview15 code. The CompactRIO 9035 chassis is used with several modules (one for reading data thermocouples, one for analog reading of the other data and one last module for generating voltages and communicating with the power supply) to acquire the data and control the heating during experiments. Two P.I.D. controllers can be used:

- A power control based on the measurement of the power ($\mathcal{P} = \mathcal{UI}$) delivered by the power supply where the gains of the P.I.D. have been determined experimentally. This P.I.D. is quite flexible to impose signals of several types on the wall and obtain a steady case with a constant power control or a transient case with either linear or exponential power evolution.
- A temperature control based on the measurement of the resistance of the metal foil that evolves with its temperature. The resistance of the foil R is a linear function of the temperature in the studied temperature range: $R = R_o + a.(T_w - T_{ref})$ where $R_o = 0.031\ \Omega$ is the resistance at the temperature of reference $T_{ref} = 50\ ^\circ$C, T_w is the metal foil temperature and $a = 7.1\ 10^{-5}\ \Omega.K^{-1}$ the coefficient of electrical resistivity. Using the resistance of the metal foil is not intrusive and almost instantaneous as the resistance is directly measured on the electrical connections of the foil. A comparison between the imposed temperature (through the measurement of the resistance of the metal foil) and the averaged wall temperature measured by infrared thermography shows that the P.I.D. correctly generates the ramp of temperatures but loses in accuracy as the heating rate increases (Fig. 3a). At high imposed temperatures, the wall temperature of the heated foil is not homogeneous anymore with the appearance of hot spots. As illustrated in Fig. 3b, for an hypothetically imposed level of temperature, the median and mean wall temperatures as revealed by IR thermography shift from this level and there exists a significant standard deviation σ_T around the median value. This has some consequences on the standard deviations of the local value of the foil resistance.

More details on these P.I.D. controllers are given in Appendix A.

2.3. Wall-to-fluid heat flux determination

The wall-to-fluid heat flux Φ_w is determined locally (for each analyzed pixel of the infrared camera picture) by considering a local energy balance of the heated wall as follows:

$$\Phi_w = \Phi_{gen} - \Phi_{sensible\ heat} - \Phi_{natural\ convection} - \Phi_{conductive\ flux} - \Phi_{radiation} \quad (1)$$

where $\Phi_{gen} = \frac{UI}{S}$ is the volumetric heating source generated by Joule effect, $\Phi_{sensible\ heat}$ is the sensible heat of the wall[1], $\Phi_{natural\ convection}$ is the heat flux transferred by natural convection from the backside of the wall in contact with air, $\Phi_{conductive\ flux}$ is the conduction along the wall and $\Phi_{radiation}$ corresponds to radiative heat flux from the black surface to the surrounding.

All the flux contributions have been estimated for different test conditions. Φ_{gen} is simply deduced from the power generator measurements. $\Phi_{sensible\ heat}$ is considered thanks to the local temperature variation rate from the IR measurements. $\Phi_{natural\ convection}$ is estimated with a Grashoff number value ranging from 10^7 to 3.10^7. $\Phi_{conductive\ flux}$ estimation is based on both azimuthal and axial temperature gradients from IR pictures. $\Phi_{radiation}$ is deduced from view factor of a concave geometry. More information can be found in Scheiff et al. [10] and Scheiff [15].

On the Fig. 4, we plotted the different contributions of the energy balance (1) for a typical transient test during nucleate boiling.

For this test, the temperature control is used to impose a rapid variation on the heat flux. It shows that, even for this type of rather transient test conditions, the generated heat flux and the sensible heat of the solid are dominant in the estimation of the wall-to-fluid heat flux with respect to other contributions. Therefore we neglect the other contributions in the rest of the analysis.

Due to the unsteady conduction through the paint layer, the sensible heat terms have to consider the layers of both metal and paint and therefore the energy balance reads:

$$\Phi_w = \Phi_{gen} - \underbrace{(\rho_w C_{p,w} e_w + \rho_p C_{p,p} e_p)}_{M_{th}} . \frac{dT_w(t)}{dt} \quad (2)$$

where M_{th} corresponds to the thermal mass.

The absolute uncertainty on the heat flux is determined as :

$$(\Delta\Phi_w)^2 = \left[\frac{\partial\Phi_w}{\partial\Phi_{gen}}\right]^2 \Delta\Phi_{gen}^2 + \left[\frac{\partial\Phi_w}{\partial e_p}\right]^2 \Delta e_p^2 + \left[\frac{\partial\Phi_w}{\partial(dT_w/dt)}\right]^2 \Delta\left(\frac{dT_w}{dt}\right)^2 \quad (3)$$

The generated heat flux varies from 40 to 400 kW.m^{-2}, and the time derivative of the wall temperature at the onset of nucleate

[1] The wall is composed of the metal foil (high resistivity and thermal conductivity) and a black paint used to improve emissivity of the wall (low resistivity and thermal conductivity)

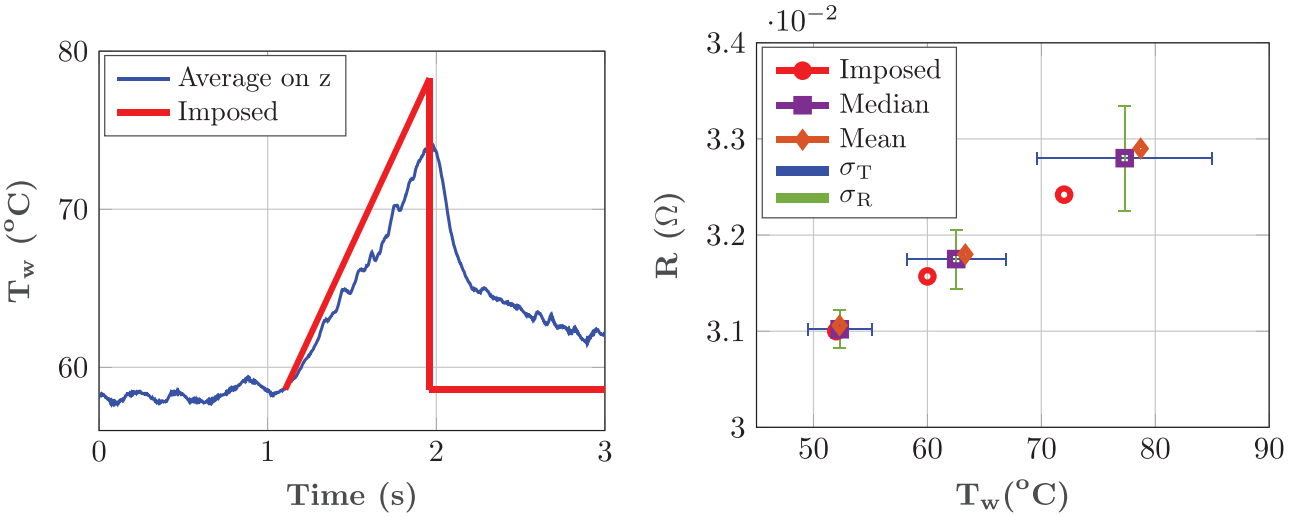

(a) Ramp = 25°C.s^{-1}

(b) Resistance of the metal foil function the wall temperature

Fig. 3. a. Generation of a temperature ramp with the P.I.D. compared to the measurement and b. Statistic analysis of the metal foil resistance with the temperature for a steady case.

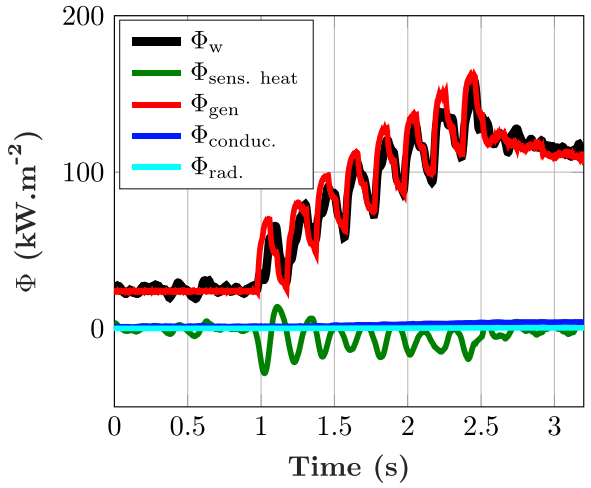

Fig. 4. Energy balance during transient nucleate boiling.

boiling varies from 10 to 500 K.s^{-1}. Due to the uncertainty on the paint layer thickness (35 $\pm$ 5 μ m), it yields a maximal 3% uncertainty on M_{th} and an uncertainty of 4.4 kW.m^{-2} on Φ_w for the most rapid transient at 500 K.s^{-1}.

So the relative wall heat flux uncertainty can reach at most 6.5%.

3. Steady nucleate boiling

In this first study, the imposed steady power level is sufficiently large to onset a nucleate boiling regime. A power step leading to a heat flux of approximately more than 40 kW.m^{-2} is sufficient to establish steady nucleate boiling. For power levels leading to heat fluxes larger than 1 MW.m^{-2}, the regime does not stabilize and a transition toward film boiling occurs. In this section, we first consider the heat transfer and then focus on bubble hydrodynamics for data obtained with three different test sections.

3.1. Heat transfer analysis

In Fig. 5, the infrared measurement of wall temperature T_w is represented for a typical test condition leading to such a steady nucleate boiling regime. On the LHS (Fig. 5.a), the wall temperature at a given z elevation is plotted as a function of time for the whole test sequence. After the first blue part of the curve, corresponding to the onset of nucleate boiling, we identified by a green circle the temperature $T_{NB,0}$ at the first time when $dT/dt = 0$. After that point, and till the power is set off (i.e. till approximately $t = 4.2$ s for this test), the red part of the curve corresponds to steady nucleate boiling. Fluctuation levels are around a few degrees with typical time variations around 0.1s. The color-level graph in Fig. 5.b shows the wall temperature along the symmetry axis of the heated foil for locations along a 4.5 cm long section and during a time sequence in the stable nucleate boiling regime (identified on the LHS graph by dotted vertical lines).

During this sequence the temperature level is relatively stable in a $[50-55]$ °C range. Some fluctuations, that are to be related to the one on the LHS graph, can be identified and their pattern is a set of quasi vertical parallel lines, indicating a coupling of the temperature time and space variation with the main flow direction (decreasing z when increasing time). These temperature fluctuations are certainly linked to the sliding of the vapour bubbles that are advected by the flow. Such vapour bubbles dynamics can be seen in fig. 7 (a) and similar quasi vertical lines are clearly visible. Obviously, the sliding of these vapour bubbles will affect the wall to fluid heat transfer and thus can be associated with wall temperature variations.

Let us define T_{NB} as the time and space averaged value of wall temperature for given test conditions, namely flowrate in terms of Reynolds number Re, subcooling in terms of Jakob number $Ja_{sub} = \frac{\rho_l C_{pl}(T_{sat}-T_l)}{\rho_v h l v}$ and imposed power level Φ_{gen} (W.m^{-2}). The results for two test sections (SE_2 and SE_3) are plotted on the curve of Fig. 6 in terms of wall-to-fluid heat flux as a function of wall superheat ($T_{NB} - T_{sat}$). Symbols identifying different flow conditions or test sections are little dispersed for the range of conditions explored. The main tendency is therefore an increase of the wall-to-fluid heat transfer with respect to wall superheat. In saturated flow boiling, a classical correlation for the prediction of the wall heat

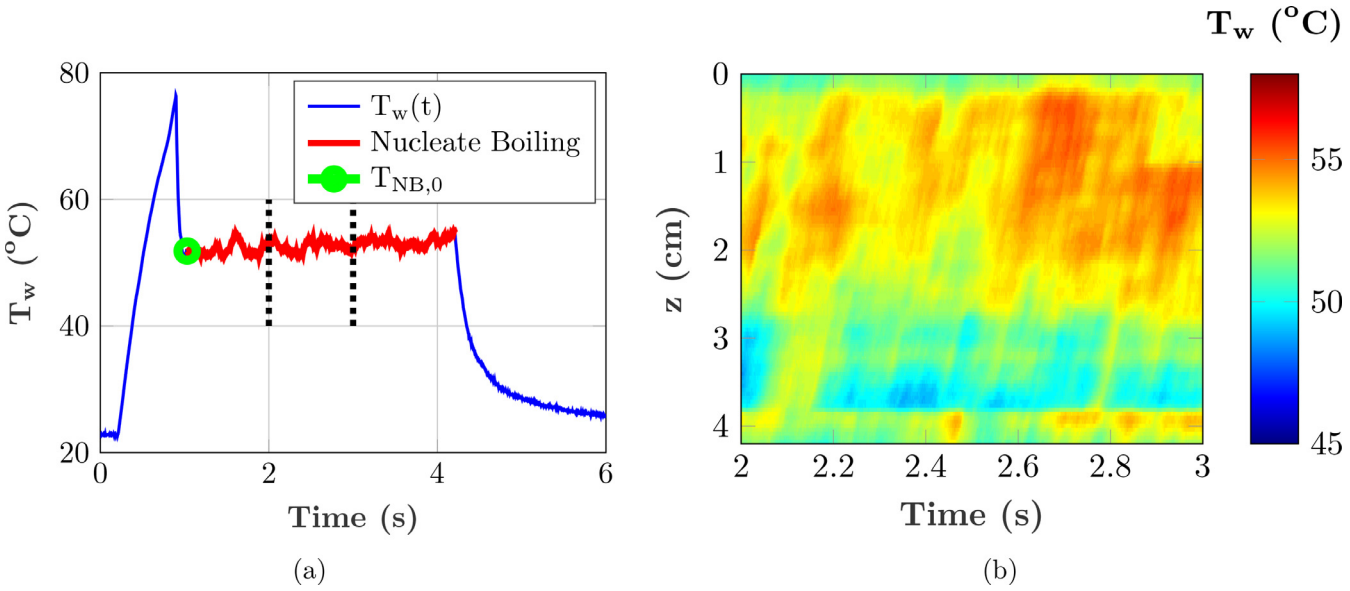

Fig. 5. a. Evolution of temperature at z=2 cm and b. Spatio-temporal curves, obtained with infrared camera measurements, of a test with imposed power to Φ_{gen} = 40 kW.m^{-2}, Re = 13 500, $\Delta T_{sub} = T_{sat} - T_l$ = 15 °C, Ja_{sub} = 22 where the nucleate boiling is fully developed. z corresponds to a vertical coordinate, the flow direction being oriented from the bottom to the top of the graph.

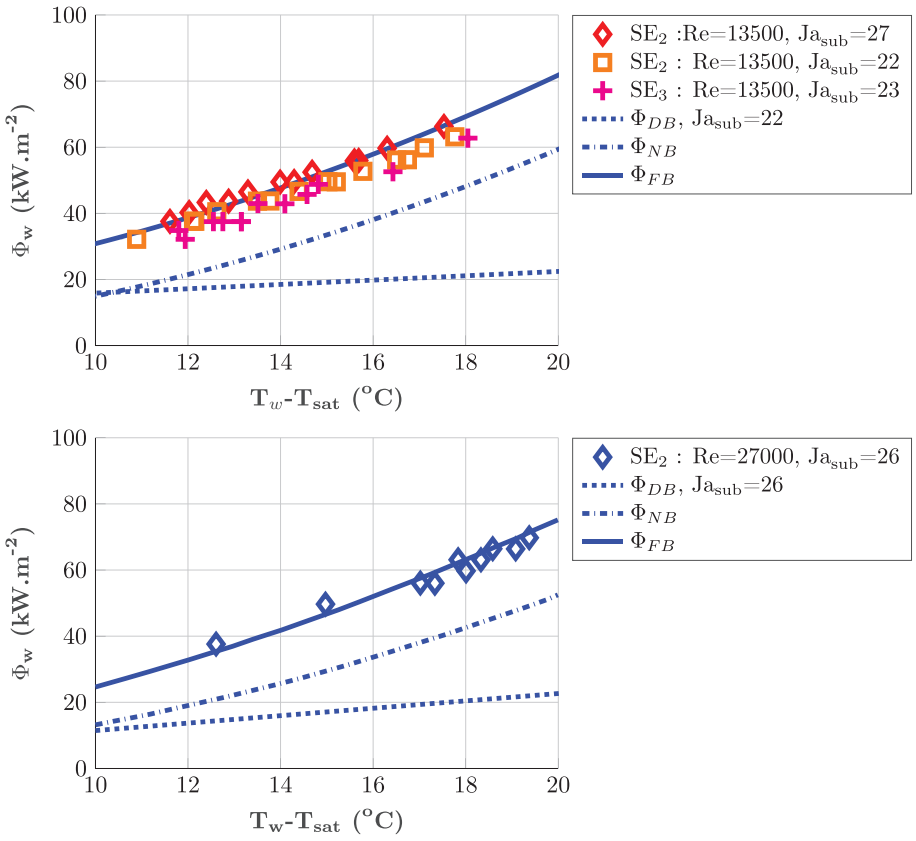

Fig. 6. a. Wall heat flux in nucleate flow boiling for Re=13 500 b. for Re=27 000, Ja_{sub} = 26.

flux has been proposed by Chen [16].

$$\Phi_{Chen} = \Phi_{DB} + S.\Phi_{FZ} \tag{4}$$

where Φ_{DB} is predicted by Dittus and Boelter [17] and Φ_{FZ} is a heat flux due to the bubble nucleation predicted by Forster and Zuber [18]. S is a suppression factor $S = \left(1 + 2.53.10^{-6}.Re^{1.17}\right)^{-1}$ proposed by Butterworth [19] (see Collier and Thome [20]). In order to take into account the liquid subcooling, a factor $S_{sub} = 1 + 3.27.10^{-4}.Ja_{sub}^2$ according to Baudin [21] is introduced in the heat flux due to nucleate boiling Φ_{NB}:

$$\Phi_{FB} = \Phi_{DB} + \Phi_{NB} \tag{5}$$

$$\Phi_{DB} = 0.023 Re^{0.8}.Pr^{0.696}.\lambda_l.(T_w - T_l)/D_h \tag{6}$$

$$\Phi_{NB} = S.S_{sub}.\Phi_{FZ} \tag{7}$$

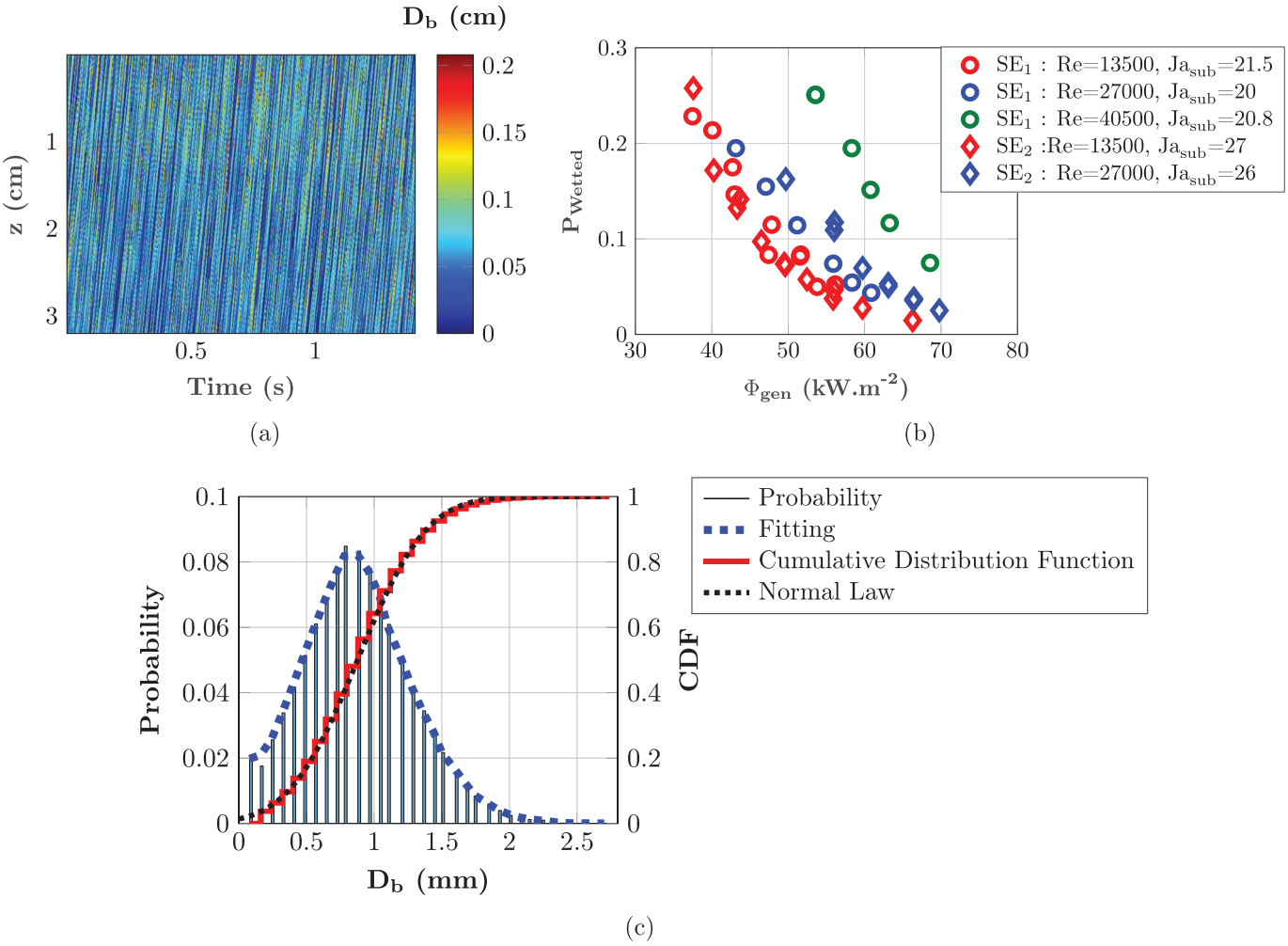

Fig. 7. a. Spatio-temporal curve of the bubble diameter obtained with the images of the high-speed camera for each location taken in the nucleate boiling zone as in the Fig. 5; b. Evolution of the fraction of wetted surface P_{wetted} depending on the generated heat flux; c. Probability density of bubble diameters with its distribution function correlated to a normal distribution law in c. The characteristics of the test are an imposed generated heat flux Φ_{gen} = 40 kW.m^{-2}, Re = 13 500, ΔT_{sub} = 13 °C, i.e. Ja_{sub}=21.5.

$$\Phi_{FZ} = A.Pr^{0.21}.La^{0.25}.\lambda_l.(T_w - T_{sat}).Ja^{0.24}/r_c \quad (8)$$

where Ja is based on the wall superheat, La is the Laplace number, r_c the radius of a vapor embryo in equilibrium for the wall superheat. A is a constant taken equal to 0.0017. For the two Reynolds number values the boiling curves reproduced in Fig. 6 are similar. Nevertheless the relative contribution of the bubble nucleation Φ_{NB} and the convective heat flux Φ_{DB} is not the same in the two cases. For Re = 13 500, the contribution of the bubble nucleation in the total heat flux is the most important, whereas for Re = 27 000, the two contributions are of the same order of magnitude. This tendency is related to the bubbly layer structure in the following section.

3.2. Hydrodynamic study

3.2.1. Bubbly layer thickness

As illustrated by the high-speed camera picture of Fig. 2, the bubbly layer in the steady subcooled nucleate boiling regime consists of a monolayer of small bubbles along the wall that covers a part of the wall. The image processing described in Section 2.1 allows to determine the thickness D_b of this bubbly layer attached to the wall for each position along the flow direction and at each time frame. Fig. 7-(a) illustrates, for a given test condition, the variation of this thickness D_b along a 3 cm long section during a 1.4s long time sequence. D_b is of the order of 0.1 cm and appears to be very homogeneous along the z direction. Space and time evolution of D_b clearly suggests some bubble path in the main flow direction. D_b values during stable nucleate boiling regime are then analyzed for a large data-set (280 000 points). From the videos during a stable nucleate boiling regime, three typical bubble size variations can be distinguished:

- The bubble grows and begins to slide along the wall. During this sliding motion the bubble diameter is almost constant as it can be seen with the inclined straight lines of the same colour (same bubble size) in Fig. 7a.
- Strong sudden growth can push the top of the bubble outside of the superheated liquid; the bubble will then condense.
- The bubble grows rapidly and is able to depart from the wall. In this case, this bubble either condenses in the subcooled flow, or stays close to the bubble layer and potentially coalesce with neighbor bubbles.

Wetted area - The lower value of the data is 0 meaning that the algorithm does not detect any bubble contour above a specific z location on the wall. According to our visual observation of corresponding pictures and to the coding of the contour detection algorithm, it means that the pixel just above the wall does not show any difference with the pure liquid case. The pixel size being 80 µm, we interpret this 0 value as the wall being locally

wetted and neglect the potential existence of very tiny bubbles below this typical size. A first analysis corresponds to the statistics of having a 0 value for the time and space range of data analyzed. It allows defining a ratio P_{wetted} whose value 1 corresponds to a non-boiling regime and whose value 0 corresponds to a wall continuously covered by a bubbly layer. For each given test condition, a single P_{wetted} value is thus defined. Fig. 7-(b) shows the P_{wetted} values for different test conditions (test section name, flow conditions in terms of Re and Ja_{sub} and power value Φ_{gen}). The tendency is clear: for given flow conditions (Re and Ja_{sub}), P_{wetted} decreases with increasing Φ_{gen}. Therefore, it corresponds to the visual observation that the wall is all the more covered with bubbles than the heat flux is large and therefore the nucleate boiling is intense. Data diverge toward 1 for sufficiently low heat flux values Φ_{gen} that corresponds to values close to the limit for the onset of nucleate boiling. Whereas the Jakob number impact seems rather low for the range investigated, the Reynolds number value clearly impacts the data: for a same wall heat flux, the larger the Reynolds number, the larger the value of P_{wetted}. Therefore the wall is all the more wetted than the bulk flow is large. This result can be linked to the thinning of the superheated fluid layer as the Reynolds number increases that will produce smaller bubbles (due to condensation at their top) that are not detected with the spatial resolution of a high speed camera. Furthermore a higher Reynolds number will induce smaller detachment diameter for the bubbles that will condense in the subcooled flow. This result can explain the tendency observed in Figs. 6a and 6b. The contribution of the heat flux due to nucleate boiling decreases as the Reynolds number increases. Nucleate boiling may be partly suppressed.

D_b distribution and mean value Let us now consider statistics concerning the thickness of the bubbly layer whenever it is detected on the wall. We therefore exclude zero D_b values (corresponding to the absence of detection of any bubble at a given time and location over the wall) from the data and consider the statistics of the remaining non-zero D_b values. The corresponding statistics correspond therefore to the size distribution of the bubbly layer over the wall and are illustrated by the graph of Fig. 7-(c). The distribution function is discretized by steps of 80 µm according to the pixel size of the high-speed camera image. This bubbly layer thickness has values lying between 0.1 mm to 2 mm and the distribution function is very well fitted by a normal distribution law. The most likely size is 0.7 mm.

D_b variation against test conditions- The mean bubbly layer thickness $< D_b >$ is plotted in Fig. 8a for various test conditions. For given flow conditions (same symbol), $< D_b >$ clearly increases with heat flux, that can be interpreted as a higher heat flux associated with latent heat transport in the overall heat transfer process. For a given wall-to-fluid heat flux, the mean bubbly layer thickness decreases with higher Jakob number or Reynolds number. Subcooling and flowrate clearly enhance condensation at the top of the bubbly layer thickness. From this previous analysis, we identify the dependency of the bubbly layer thickness with respect to three main parameters as being, the boiling number $Bo = \frac{\Phi_{gen}}{h_{lv}.G}$ that scales the heat flux with the heat transfer sufficient to vaporize the entire liquid mass flux, the Reynolds number Re and the Jakob number Ja_{sub}. Let us note that from the visual observation of the high speed camera pictures, the bubbly layer is clearly mono-layer. We then refer to the work of Zeitoun and Shoukri, [22] that empirically derived a correlation for the Sauter mean diameter of bubbles on a vertical wall with water flowing in an annular section at low pressures. In their study, they also observed a mono-layer of bubbles and their sizes are measured thanks to a high-speed camera that films bubbles from above. We therefore consider fitting our data thanks to Zeitoun and Shoukri's correlation. In our experiment, both fluid and flow section geometry differ from Zeitoun and Shoukri's work. The parameters (empirical coefficients appearing in the formula including exponents of the power laws) of this correlation have been adjusted by the least squares method. The fitted correlation then reads:

$$\frac{\langle D_b \rangle}{L_c} = \frac{0.69\left(\frac{\rho_l}{\rho_v}\right)^{1.76}}{Re^{0.54}\left[Ja_{sub} + \frac{165.9\left(\frac{\rho_l}{\rho_v}\right)^{1.76}}{Bo^{0.75}.Re^{1.73}}\right]} \tag{9}$$

with $L_c = \sqrt{\frac{\sigma}{g\Delta\rho}} \sim 0.9$ mm corresponding to the capillary length. Please consider that, since we did not vary the pressure, the additional non-dimensional number considered by Zeitoun and Shoukri [22] as the density ratio ρ_l/ρ_v is constant in our experiments and that we kept the same 1.76 power coefficient in the correlation.

The comparison of this correlation with the experimental results for different parameters and test sections is represented in the Fig. 8b. This correlation correctly approaches our measurements in the range $\Phi_{gen} \in$ [35- 90] kW.m^{-2} which corresponds to boiling number $Bo \in [4.10^{-4} - 2.10^{-3}]$, $Re \in$ [13 000 - 41 000], $Ja_{sub} \in$ [20 - 30]. The difference between the model and the experimental results remains rather small on the range of our parameters (lower than 15%), considering that the bubble diameter distributions are quite large in our experiments. However,this correlation seems to over-predict the smallest bubble diameters and to under estimate the largest ones. We therefore proposed a best fitting of our experimental data versus Bo, Re and Ja_{sub} numbers:

$$\frac{D_b}{L_c} = \frac{49.419 + 5.846 BoRe}{Re^{0.3} Ja_{sub}^{0.7}} \tag{10}$$

The comparison of this correlation with respect to our experimental data is plotted in Fig. 8c and shows to agree better with our data than the adaptation of Zeitoun and Shoukri correlation. Our proposed correlation depends on the parameters Φ_{gen}, G and $T_{sat} - T_l$ independently through the dimensionless numbers $BoRe$, Re and Ja_{sub}, respectively. It allows to consider the following correlations between individual parameter variation:

- When the heat flux increases, only the $BoRe$ value increases and the bubble diameter increases
- When Ja_{sub} increases, the denominator of the equation will increase thus decreasing the bubble diameter, which is consistent with the fact that the strong subcooling results in smaller bubble diameters.
- As the mass flux increases, the Reynolds number increases, the denominator of the equation will increase thus decreasing the bubble diameter. This result confirms the decrease in the bubble size with increasing the flow velocity.

3.2.2. Bubbles velocity

From visual observation, see e.g. Fig. 2, many vapor bubbles are present along the axis of symmetry of the foil and slide along the wall in the main flow direction. Let us consider the analysis of their velocity. Bubble velocity on raw images of the high-speed camera are complicated to determine from an image processing based on a Lagrangian tracking of particles mainly because they are so close from each other that a contour recognition does not easily identify individual particles. Nevertheless, oblique and parallel lines are distinguished clearly in Fig. 9.a: those lines are trajectories of the patterns of the bubbly layer that we assume to correspond to bubble paths.

To quantitatively estimate the velocities along the trajectories, an algorithm that tracks these oblique lines slopes on the experimentally measured D_b(z,t) fields (like Fig. 9.a) has been developed. Trajectories are identified thanks to samples of tracked correlations in the space and time diagram of bubbly layer thickness $D_b(z, t)$.

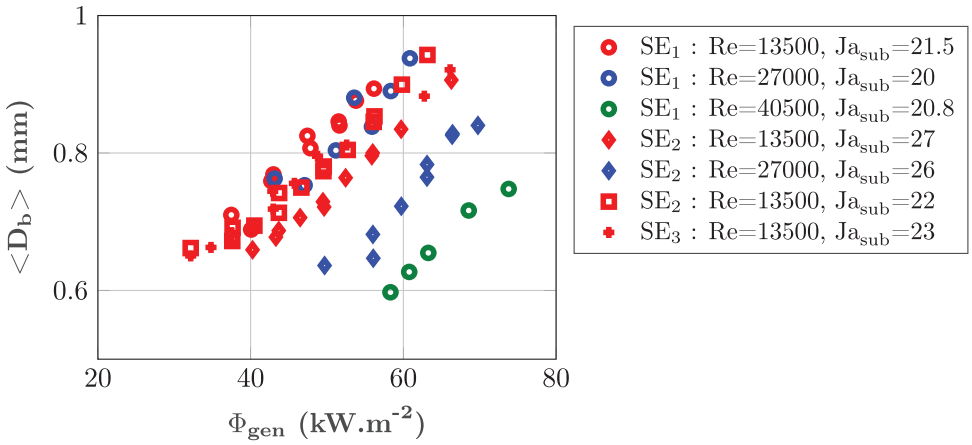

(a) $\langle D_b \rangle$ variation against test conditions

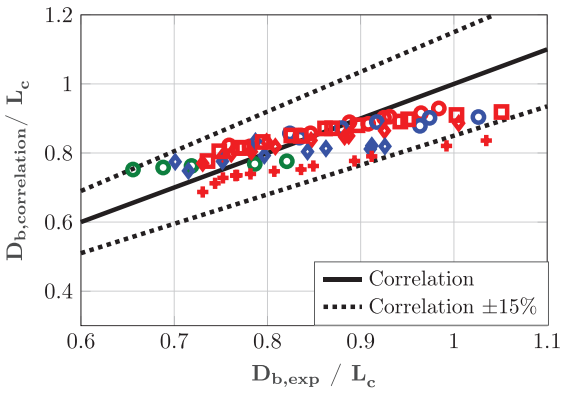

(b) Experimental $\langle D_b \rangle$ *vs* Zeitoun and Shoukri [22]'s correlation.

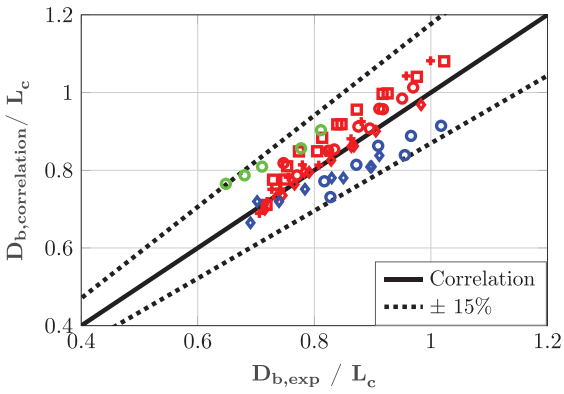

(c) Experimental $\langle D_b \rangle$ *vs* authors' correlation.

Fig. 8. Mean bubbly layer thickness $< D_b >$ for different experimental conditions.

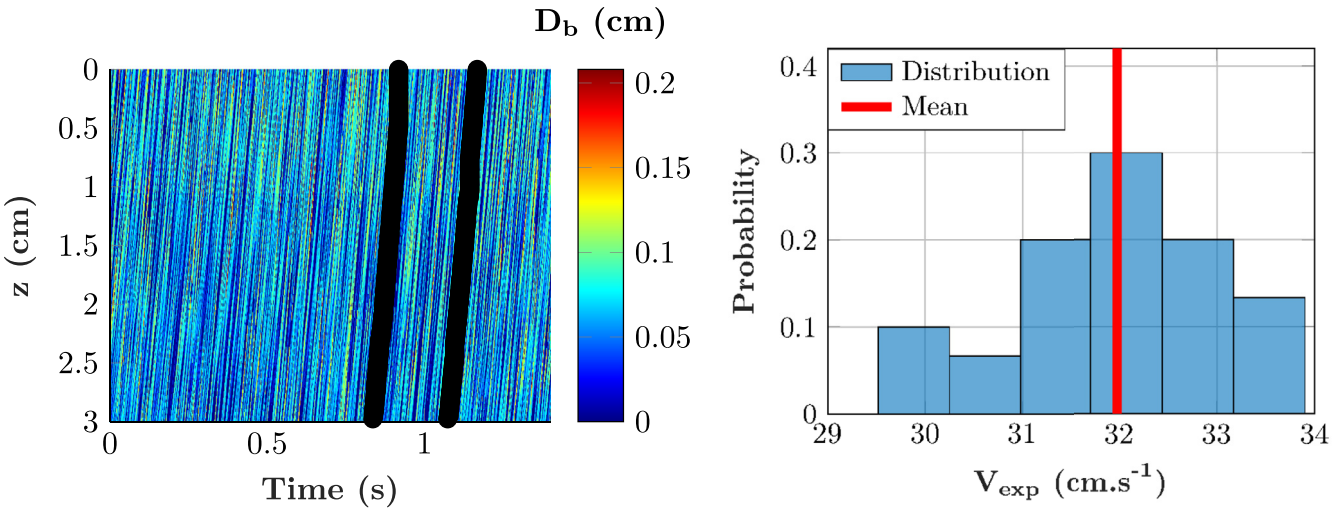

(a) (b)

Fig. 9. a. Trajectories of bubbles obtained in two different zones (black lines) on a spatio-temporal curve and b. Probability density and average velocity obtained for 30 tests in (b) with SE1 : Re = 13 500 and ΔT_{sub} = 13°C, Ja_{sub}=21.5.

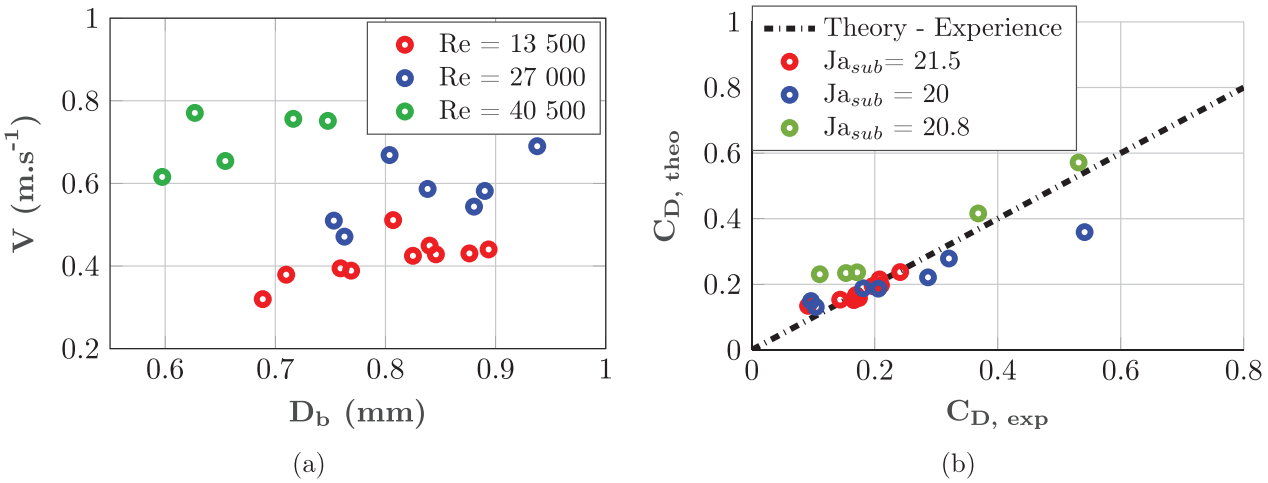

Fig. 10. a. Experimental velocity determined for bubble diameter range of 0.6 to 1 mm on SE1 and b. Comparison of the experimental drag coefficients with the theoretical values obtained by Shi et al. [1].

Tracking algorithm is as follows. First a starting point is randomly selected across non-zero values in the order of magnitude of the mean bubble size along the bottom line of the diagram (lower position z_0 along the flow direction). It corresponds therefore to a given value $D_b(z_0, t_0)$ of the diameter at a specific time t_0. Surrounding D_b values are then filtered thanks to a weighting function $p(z, t)$, an Euclidian transformation that equals the distance with respect to (z_0, t_0) till an arbitrary threshold value and cancels over this value. The next position of the tracked trajectory is identified as the maximal value of $p(z, t)^*D_b(z, t)$, that is (z_1, t_1), in the neighborhood of (z_0, t_0). The process is then repeated till either $z = zmin$ at the top (here $zmin = 0$cm) of the diagram or $t = tmax$ at the right hand side of the diagram (here $tmax$ =1.5s). The obtained trajectories are relatively straight lines, parallel to the pattern visually seen on the diagram as illustrated by the two black lines on Fig. 9 a. For given test conditions, 30 different trajectories are randomly selected. For each trajectory, the average slope is then determined and associated to the bubble velocity along the wall V_{exp}.

Statistics on V_{exp} values for a given test condition are represented in Fig. 9.b as a probability density function over $\simeq$ 0.5 m.s^{-1} width intervals. Scattering around the mean value (indicated by the red line) is rather low.

The mean bubble velocity V is plotted versus the mean bubble diameter D_b for different test conditions in Fig. 10a. This velocity increases with the bubble diameter and with the liquid velocity. The bubble relative velocity $V_R = V - u$ can also be calculated, u being the liquid velocity at the position of the center of gravity of the bubble $D_b/2$. The velocity profile in the semi-annular gap close to the inner cylinder is calculated from the logarithmic law given by Kaneda et al. [14]

$$u^+ = \frac{u}{u_*} = A + \frac{1}{\kappa}\ln(y^+) \tag{11}$$

$$y^+ = \frac{\rho y u_*}{\mu} \tag{12}$$

where y is the distance to the wall, $u_* = \sqrt{\frac{\tau_W}{\rho}}$ is the friction velocity. The wall shear stress τ_w has been measured by Baudin et al. [9]. The constant A is estimated by Kaneda et al. as A=6.13 and κ is the von Karman constant κ=0.436.

The relative bubble velocities range from 0.1 m.s^{-1} to 0.3 m.s^{-1}. From the measurement of the bubble relative velocity it is possible to determine the drag coefficient C_D on the bubbles from a balance between the buoyancy force F_B and the drag force F_D:

$$F_B + F_D = 0 \tag{13}$$

$$F_D = -\rho\frac{\pi(D_b/2)^2}{2}C_D V_R^2 \tag{14}$$

$$F_B = \frac{\pi D_b^3}{6}(\rho_l - \rho_g)g \tag{15}$$

The drag coefficients obtained experimentally from the measurement of V_R are compared to the theoretical expression derived by Shi et al. [1] from numerical simulations of a sliding bubble in a shear flow in a wall vicinity:

$$C_D = C_{D0}(1 + \Delta C_D^W) \tag{16}$$

$$\Delta C_D^W = 0.47L_R^{-4} + 0.0055L_R^{-6}Re_b^{3/4} + 0.002S_R^{1.9}Re_b + 0.05L_R^{-7/2}S_R Re_b^{1/4} \tag{17}$$

where $Re_b = \frac{2(D_b/2)V_R\rho}{\mu}$, $L_R = 2L/D_b$, L being the distance between the center of gravity of the bubble and the wall, $S_R = \gamma D_b/V_R$ is the dimensionless shear rate, $\gamma = du/dy$ and C_{D0} is the drag coefficient of Mei and Klausner [23] for a spherical bubble in a quiescent liquid and unbounded medium:

$$C_{D0} = \frac{16}{Re_B}\left(1 + \left(\frac{8}{Re_B} + \frac{1}{2}\left(1 + \frac{3.315}{\sqrt{Re_B}}\right)\right)^{-1}\right) \tag{18}$$

The experimental drag coefficients plotted in Fig. 10b are in good agreement with the theoretical expression extrapolated for $L_R = 1$. One discrepancy is observed for the largest value of C_D which correspond to the highest values of the dimensionless shear rate $S_R >$ 0.8 out of the range of the numerical simulations by Shi et al. [1] performed for $S_R \leq$ 0.5. The good prediction of the bubble relative velocity for a large range of heat fluxes and Reynolds numbers is of great interest for the elaboration of an advanced heat transfer model based on heat flux partitioning. The effect of the bubbles' sliding along the wall in vertical flow has namely an important contribution in the total heat flux transferred to the fluid (Basu et al. [24]).

3.3. Imposed temperature

With the help of the P.I.D. control system, it is possible to impose constant wall temperatures and therefore deduce boiling curves. First, a spatio-temporal diagram of the temperature is given

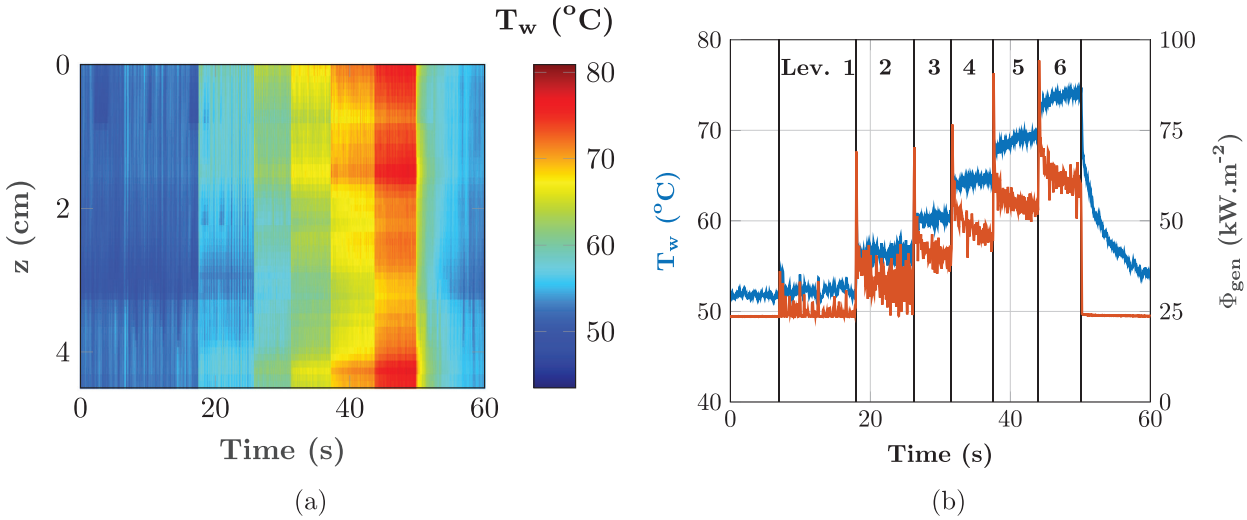

Fig. 11. a. Spatio-temporal temperature diagram of the nucleate boiling regime when the temperature is imposed and b. Axial average of T_w with generated heat flux synchronization, Re = 13 500, ΔT_{sub} = 14 °C, Ja_{sub}=22.

Fig. 11.a.The different temperature levels are easily identifiable here with delimited areas in time. The heat flux generated by the P.I.D. to obtain these constant temperatures is shown in Fig. 11.b. The results are determined on one test section called SE_4.

The control system P.I.D. correctly follows the instructions: the temperature average in the foil (measured from the resistance of the foil) is constant even for the highest values. The overheating obtained can be of the order of 40 °C or more. These temperature levels are particularly high for a nucleate boiling regime and cannot be classically reached for constant power level controls. It allows describing the nucleate boiling process at higher wall superheats in steady conditions. At each set-point level, an overshoot on the generated heat flux is observed then a relatively fast stabilization towards a constant generated flux is reached. In order to characterize the complexity of the transient regime, the probability density function of the wall temperature for each temperature level, is estimated. Frequency acquisition of the infrared camera is 500 Hz and each temperature level lasts on average 5 seconds.

In order to investigate the wall temperature distribution at a steady temperature level, a similar analysis to Golobič and Zupančič [11] is performed. There are 2500 images in total, which makes a total of 3,300,000 temperature points for each constant temperature step. The probability density as well as the cumulative distribution function (CDF) are calculated for three levels of temperature plateau in the Fig. 12 a-c (corresponding to #1, #3 and #6 test conditions of Fig. 11). The CDF (in orange on the curve) is an average of each CDF determined for each time step. The difference is less than 1% and so remains stable in time to be able to consider an average CDF.

Nucleate boiling is fully developed on the wall, yet the densities of probabilities in Figs. 12 (a-c) show one peak followed by a temperature tail. A first temperature peak that corresponds to the set temperature and a tail where the temperatures are higher and correspond (from an IR pictures analysis) of several different localized areas. These, so called, hot spots are thus interpreted as being either areas where boiling has not been triggered (for low temperatures Fig. 12.a and.b), or zones of intense vaporization (close to the vapor film) which insulate the wall of the liquid (valid at high temperatures, Fig. 12.c). In this latter case, higher is the imposed temperature, the more these areas appear and disturb the thermal system. These hot spots are the same for each distribution and are precursors for the film boiling establishment. As previously pointed out in Fig. 3b, it becomes more difficult to reach the imposed resistance, through the P.I.D. control of the system when the temperature is high.

A spatio-temporal diagram of the heat flux transferred to the liquid is determined from the spatio-temporal diagram of the temperature (Fig. 11) and is illustrated in Fig. 13.a. The wall to fluid heat flux appears not to depend on the z position for each imposed temperature level. Fig. 13.b is a local boiling curve (taken in the middle of the section test).The different overshoots in the Fig. 13.b come from the P.I.D. and are characteristics of its regulation parameters to adapt the flux to the temperature set point. In our tests, to maintain the constant temperature to the set-point, the P.I.D. quasi-instantaneously adapts the power that leads to overshoot in heat flux at the time of changing the set-point as shown in Fig. 11. For each step in temperature during a typical test, the overshoot lasts a few ms before stabilization. The flux and the temperature have a high variability during each imposed temperature level but it is always possible to extract a classical average boiling curve by averaging the wall to fluid heat transfer on each axial position z for each temperature level. This yields to the fitted curve on Fig. 13.b.

The standard deviation between the average boiling curve and the local one is only 2.5% for this test. Similar standard deviations are obtained for all the test performed and thus average boiling curves can be compared to those resulting from imposed power tests. On Fig. 14, we plotted with lines the boiling curves obtained for different flow rates conditions: it shows very little impact of the Reynolds number value on the wall-to-fluid heat flux. The same trend previously obtained for the imposed power tests is thus recovered.

3.4. *Power* vs *temperature*

Power control and temperature control of the system are compared on the same boiling curve on the Fig. 14.

For the same flux transferred to the liquid, the overheating at the wall is more important during temperature control: heat exchanges are therefore relatively degraded. To keep constant overheating as intense as possible, the control system has to adapt the generated heat flux quickly and irregularly to avoid boiling transient nucleus. The establishment of P.I.D. changes for each test section and especially the temperature levels are not identical. Indeed for significant overheating, the resistance of the foil is not necessarily linear with the temperature, which implies that the P.I.D. takes a little more time to react. Because of these settings

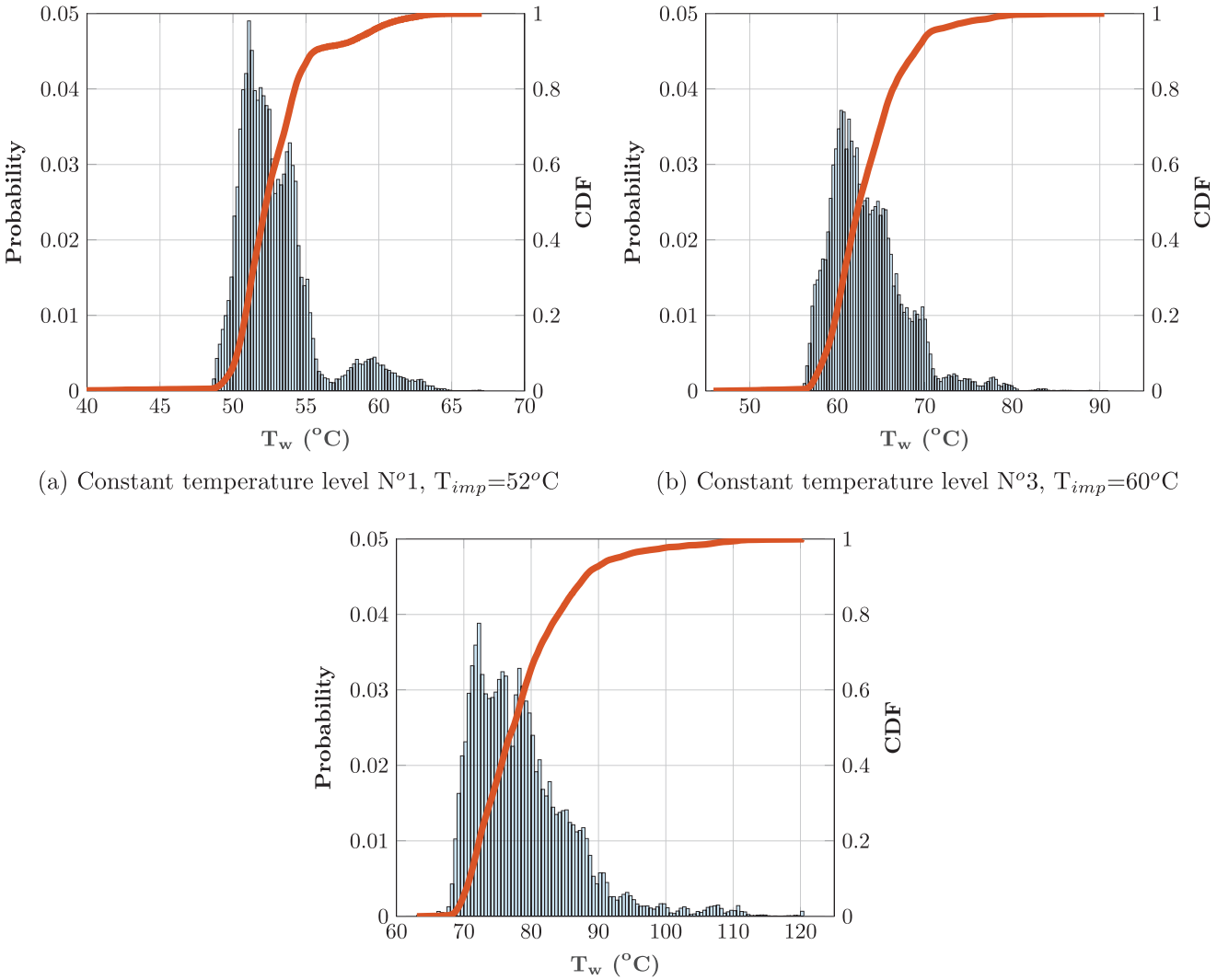

(a) Constant temperature level N°1, T_{imp}=52°C

(b) Constant temperature level N°3, T_{imp}=60°C

(c) Constant temperature level N°6, T_{imp}=72°C

Fig. 12. Statistical study on the temperature field.

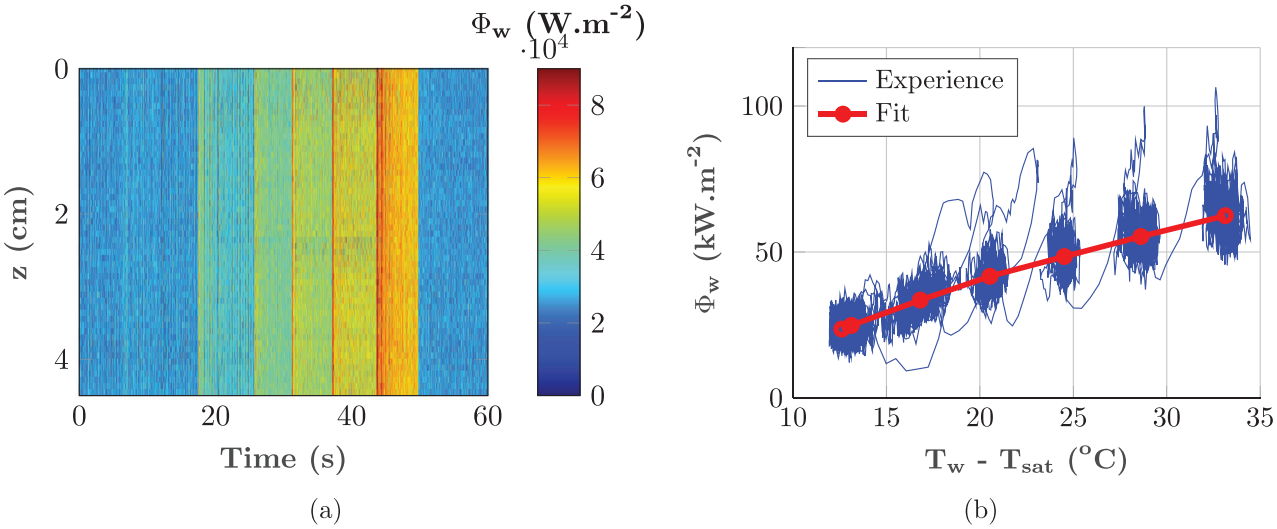

(a)

(b)

Fig. 13. a. Spatio-temporal diagram for the heat flux transferred to liquid during nucleate boiling regime when the temperature is imposed and b. Local boiling curve with the averaged heat flux on a test where Re = 13 500, ΔT_{sub} = 14 °C, Ja_{sub}=22.

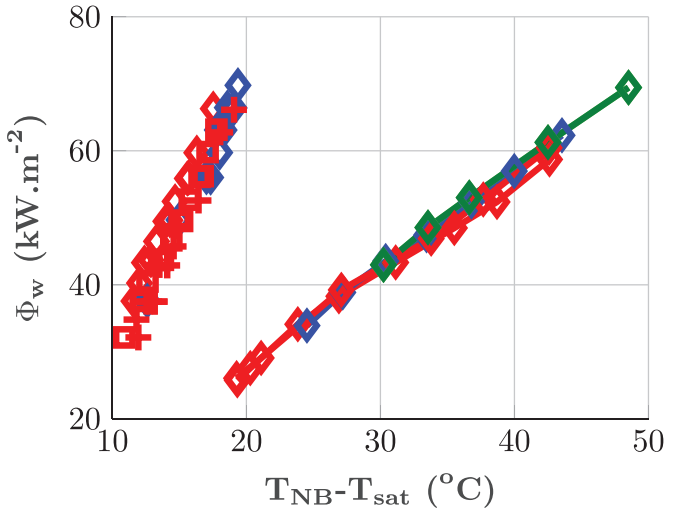

Fig. 14. Boiling curves with power control (point) and temperature control (solid line) depending on the overheating at the wall for several flows (red = 13 500, blue = 27 000, green = 40 500) and subcoolings (ΔT_{sub}: □ / + = 15 °C,◇ = 17 °C, line-◇ = 14 °C and Ja_{sub}: □ / + = 22,◇ = 27, line-◇ = 22.) . (For interpretation of the references to colour in this figure legend, the reader is referred to the web version of this article.)

in particular, the temperature, and thus the flux generated, will go through a transitional phase before stabilizing. A specificity of the temperature control results is thus a high scattering of power and temperature values around their mean value retained for comparison with power control results. We did not identify some correlation between instantaneous temperature and heat flux value and therefore can not rely on these fluctuations to any specific boiling mechanism that could help interpreting the difference in heat transfer efficiency with respect to more stable cases of power control. Perspectives could be to analyze more deeply those fluctuations, attempting to identify some frequencies, but also to observe synchronized high speed camera to see whether those thermal fluctuations could be related to some specific events within the bubbly layer.

4. Transient nucleate boiling

High-speed temperature ramps are imposed thanks to the P.I.D. The different ramps can be either low from 1 to 50 K.s^{-1}, and thus be compared to the tests of Auracher and Marquardt [2], or steeper from 50 to 500 K.s^{-1}, to obtain fast transients closer to the phenomena observed during a RIA. Plots of Fig. 15 illustrate time and space wall temperature variations for different P.I.D. setups yielding to low ramps for a Reynolds number value of 27 000 and a subcooling $\Delta T_{sub} = 14$ °C.

A comparison between the imposed temperature (through the value of average resistance of the foil on its length) and the average temperature measured by Infrared Thermography shows that the P.I.D. correctly generates constant temperature increase rates (Fig. 15 d-f). However, the higher the desired temperature ramp, the lower the accuracy of the P.I.D. Figs. 15 show that taking an average of the temperature does not allow to represent all the phenomena (boiling incipience, hot spot formation,...) that can appear on the wall. It is necessary to take into account the standard deviations to ensure intervals of trust for all tests. This standard deviation is at most 2 °C: this low value allows us to consider an axial average. The results obtained for several temperature ramps are shown in Fig. 16.

The resulting wall temperature ramps as recorded by the IR camera are plotted in Fig. 16. The acquisition frequency of the infrared camera is equal to 500 Hz and the fastest test lasts 0.05 s, which produces 25 frames during the temperature ramp. The characterization of the heat transfer at these high heating rates is therefore possible experimentally but a little less accurate.

4.1. Comparison of steady and transient heat fluxes

The boiling curves (heat flux versus wall superheat) are plotted for transient nucleate boiling and compared to the steady state in Fig. 17.

The results show that the higher the heating rate, the higher the heat flux transferred to the fluid. These results are qualitatively similar to those of Auracher and Marquardt [2].

Curves have a common starting point (the beginning of the ramp) thanks to a normalization with respect to the initial Φ_w value (all tests begin from approximately the same condition), noted $\Phi_{NB,0}$. This value corresponds to the heat flux in the steady nucleate boiling regime with imposed wall temperature $T_{NB,0}$ preceding the temperature rise linked to the heating rate at t_{NB}. Note that $\Phi_{NB,0}$ corresponds to the generated heat flux which is also equal to the heat flux transferred to the fluid in steady state. It appears that the time evolution is all the more steep than the ramp is steeper, the inflexion changing from concave to convex for the steepest ramps. The time evolution of the wall-to-fluid heat flux during a ramp can be then estimated.

The tests last between 0.5 s (for the steepest ramp) and 2.5 s (for the lowest). The P.I.D. imposes, at very short times, a rapid increase of the generated heat flux before reaching a lower increase rate. The ratio $\Phi_w/\Phi_{NB,0}$ increases with the heating rate. This ratio can be fitted by a power law that depends on a characteristic time scale τ of the transient heating according to:

$$\frac{\Phi_w(t, dT/dt, Re, Ja)}{\Phi_{NB,0}} = \left(\frac{t - t_{NB,0}}{\tau}\right)^{A_0(Re,Ja)} + 1 \qquad (19)$$

A_0 is a variable that depends, a priori, on the parameters of the experimental system, Reynolds number and Jakob number based on the subcooling of the flow. It is specified here that the influence of subcooling could not be studied in the context of this experimental campaign. To reduce the variability associated with the specificity of each test section, evolutions are presented for the same test section.

In Fig. 18 the fitted value of the parameters τ and A_0 are plotted against the main parameter of the ramp, namely dT/dt. For the lowest ramps, τ and A_0 are clearly correlated to dT/dt, while trends can not be inferred for steepest ramps and the fitting by a power law (19) does not seem relevant. For the lowest ramps, the value of A_0 is always larger than 1 that leads to time evolution that is consistent with the previous remarks. For the lowest ramps, τ is clearly a decreasing function of dT/dt that can be well fitted by a $1/x$ law. Therefore, the typical time scale for the heat flux variation is clearly related to the typical time scale of the temperature ramp.

This motivates to model the heat flux variation with respect to instantaneous temperature value rather than with time. For the lowest ramps, the variation of wall temperature with time obeys the linear law:

$$T_w = \frac{dT}{dt}(t - t_{NB,0}) + T_{NB,0} \quad \Rightarrow \quad t - t_{NB,0} = \frac{(T_w - T_{NB,0})}{\frac{dT}{dt}} \qquad (20)$$

Thus the heat flux transferred to the liquid can be modeled by:

$$\Phi_w = \Phi_{NB,0}\left(\frac{T_w - T_{NB,0}}{dT/dt}\frac{1}{\tau}\right)^{A_0(Re,Ja)} + 1 \qquad (21)$$

4.2. Comparison with Auracher and Marquardt

A comparison between the model and the experimental results is given in Fig. 19 a. for our experiments and in Fig. 19 b. for the

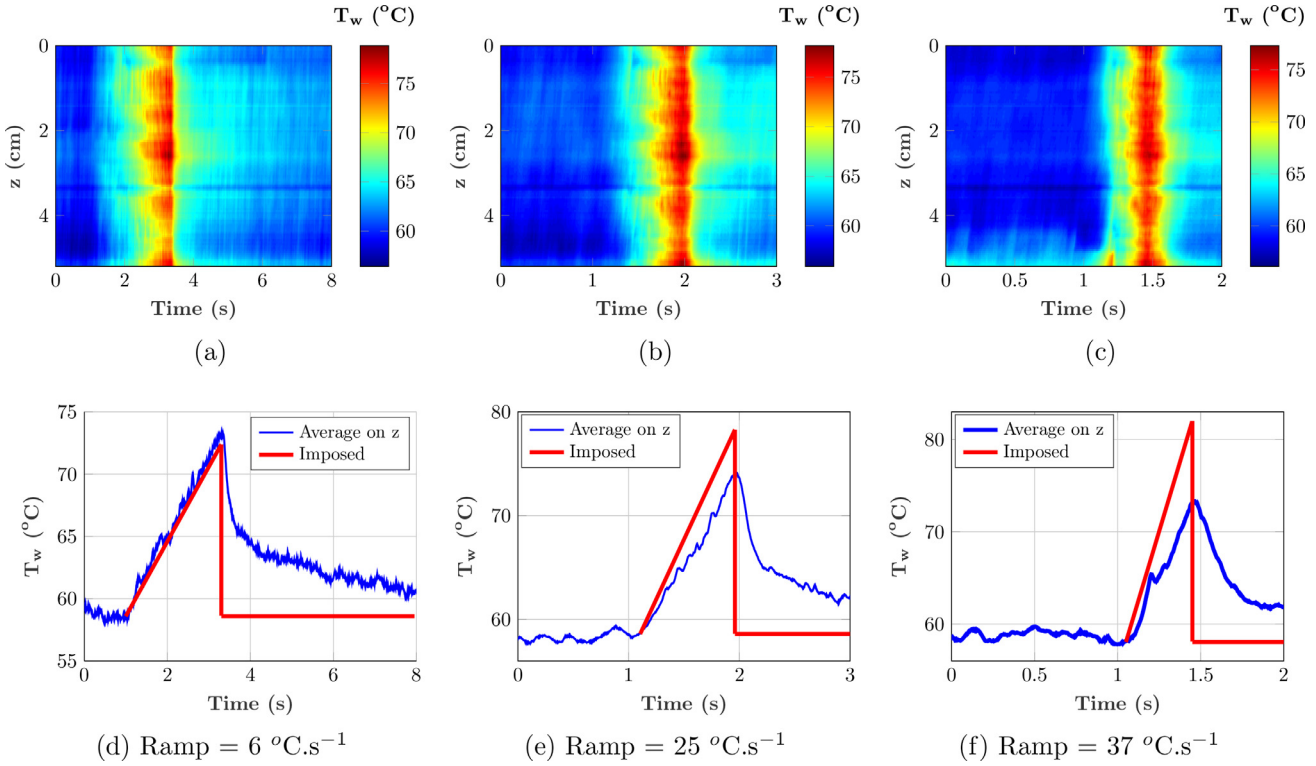

Fig. 15. a-c. Spatio-temporal field of the wall temperature at the center of the foil for several temperature ramps. d-f. Comparison between mean wall temperature (set value in red) and the temperature deduced from the resistance of the foil (in blue). With Re = 27 000, ΔT_{sub} = 14 °C, Ja_{sub}=22. (For interpretation of the references to colour in this figure legend, the reader is referred to the web version of this article.)

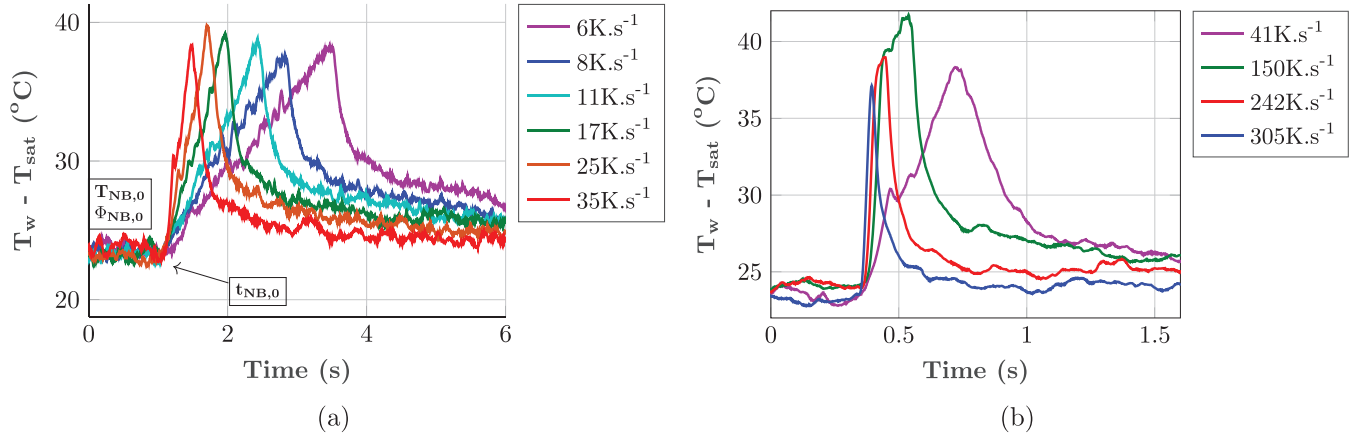

Fig. 16. a. Slow temperature ramps and b. Steep ramps as measured by the infrared camera for Re = 27 000 and, ΔT_{sub}=14 °C, Ja_{sub}=22. (For interpretation of the references to colour in this figure legend, the reader is referred to the web version of this article.)

experiments of Auracher and Marquart. The model correctly describes the heat flux for heating rates lower than 50 °C.s^{-1}. The values of the fitting parameters: characteristic time scale and constant A_0 are displayed in Table 2 for the two studies. The tests of Auracher and Marquardt and our tests can be approached with the same characteristic time scale found in Fig. 18 because both experiments are performed with the same heating rates. However, the ratio between the heat flux in the transient heating and in steady state evolves differently in Auracher and Marquardt experiments and in ours. In both experiments, the initial condition is a steady nucleate boiling regime at a constant temperature $T_{NB,0}$, but the initial heat flux $\Phi_{NB,0}$ is much lower in our experiments. In the condition of an imposed wall temperature, the heat flux is much smaller than with an imposed power as pointed out in Fig. 14. This initial condition may explain why the heat flux in transient boiling in our experiments is much smaller than that of Auracher and Marquardt. The 2 experiments also differ by the thermal inertia of the

Table 2
Comparison of the characteristic time scales and the parameter A_0 between our experimental results and Auracher and Marquardt study [2].

dT/dt	τ_{exp}	τ_{AM}	$A_{o,exp}$	$A_{o,AM}$
10	0.83	0.66	1.22	0.49
15	0.55	0.56	1.38	0.59
20	0.4	0.38	1.52	0.63
30	0.26	0.23	1.72	0.65
40	0.19	0.19	1.83	0.56
50	0.15	0.17	1.84	0.54

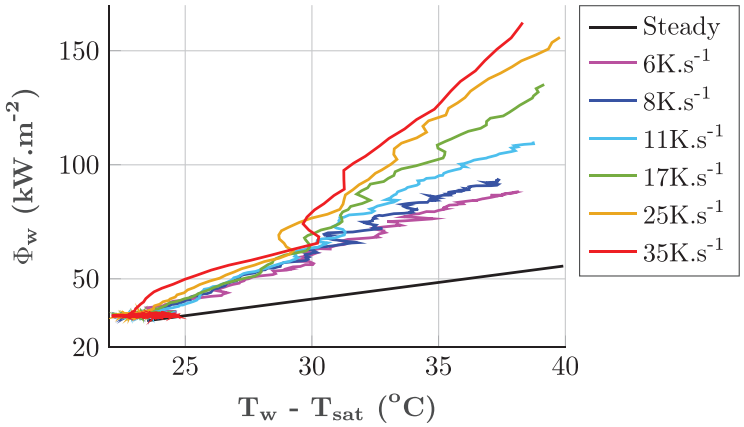

Fig. 17. Comparison between the steady and transient case for Re = 27 000 and, ΔT_{sub}=14 °C, Ja_{sub}=22.

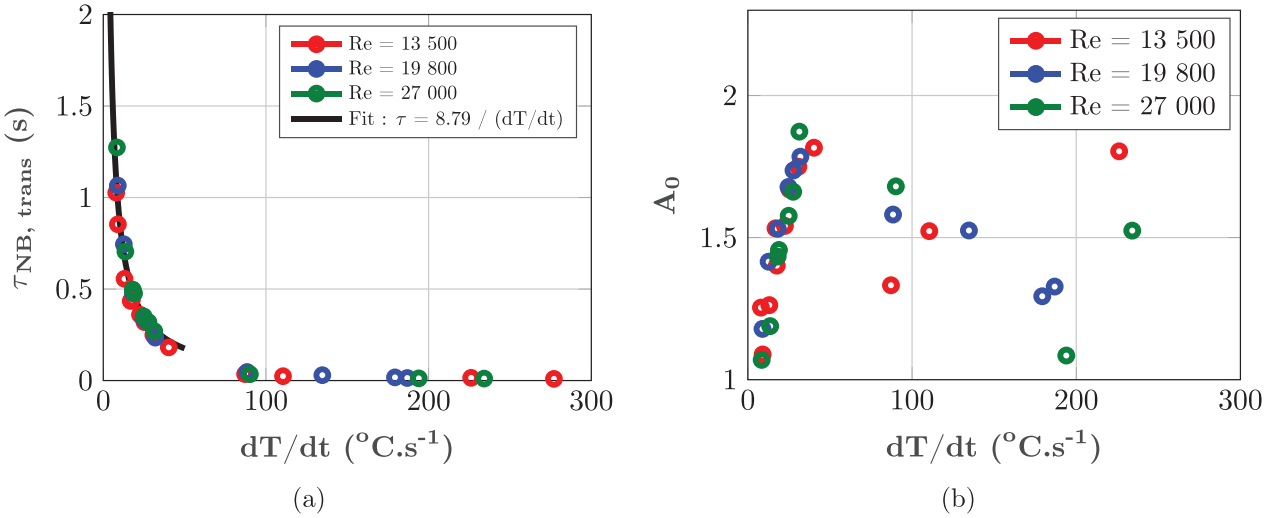

Fig. 18. a. Characteristic time scale τ and b. Experimental variable A_0 : Parameters of the model according to several Reynolds number Re and imposed heating rates dT/dt, for ΔT_{sub}=14 °C, Ja_{sub}=22.

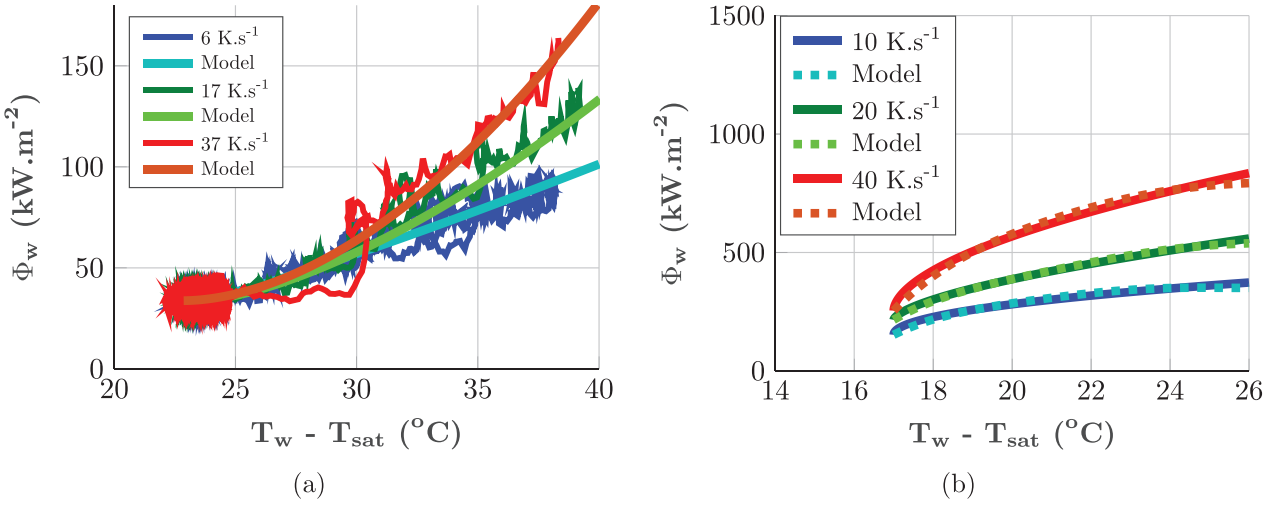

Fig. 19. a. Comparison of the model with the experimental results obtained during the test campaign and b. Auracher and Marquardt data.

heated wall. In our experiments the heater wall is only 50 µm thick whereas in Auracher and Marquardt experiments a copper block of 5mm is used with a much higher thermal inertia. Then the boiling curves evolution do not have the same concavity in the two experiments and the constant A_0 is higher for our experiments.

5. Conclusion

In steady nucleate subcooled boiling regime with a constant heating power, the wall heat flux can be predicted by the combination of the heat transfer due to forced convection and nucleate boiling. A modification of Chen correlation is proposed and allows to point out that the relative contribution of the heat flux due to convection increases with the Reynolds number while the one due to bubble nucleation decreases. This tendency is consistent with our observation of the bubbly layer: the part of the surface covered by the bubbles decreases as the Reynolds number increases. The diameters of the bubbles sliding along the wall are measured by image processing and are well predicted by a correlation based on the Reynolds, Jakob of subcooling and Boiling numbers. The velocities along the bubble trajectories are measured allowing the estimation of their relative velocity. These relative velocities are between 0.1 $m.s^{-1}$ and 0.3 $m.s^{-1}$. A drag coefficient for the sliding bubbles has been calculated from a force balance and is in good agreement with the recent numerical simulations of spherical bubble motion in a shear flow near a wall performed by Shi et al. The results obtained on the characterisation of the bubble layer: bubble diameter, velocity, portion of the surface covered by the bubbles are of a crucial interest for the improvement of the prediction of heat transfer in subcooled nucleate boiling. Namely the most advanced models based on heat flux partitioning require these data.

Steady boiling is then studied with a set constant temperature. Under these conditions, strong heterogeneities on the temperature field are observed, especially with the apparition of hot spots. The heat transfer is strongly degraded by comparison with heating by a set power. The specificity of the temperature control results is a high scattering of power and temperature values around their mean values. A further analysis of these fluctuations synchronised with the high-speed images would be necessary for a better understanding of the physical mechanisms.

Transient boiling is also studied by imposing high constant temperature increase rates thanks to the dedicated P.I.D. control system. The results are similar to those obtained by Auracher and Marquardt. The wall heat flux increases with the heating rate dT/dt. For heating rates below 50 $^{\circ}C.s^{-1}$, the heat flux time variation scaled by the heat flux in steady boiling is well fitted by a power law of a dimensionless time t/τ. The time scale τ is inversely proportional to the heating rate for both our experiments and the experiments of Auracher and Marquardt. The exponent of the power law A_0 differs in the two studies. It depends on the flow parameters (Reynolds number and subcooling) and the steady boiling regime preceding the temperature ramps. Finally a correlation for the wall heat flux in transient nucleate boiling regime versus the wall superheat is provided.

Additionnal material

Some flow visualisations are available on the website: https://www.irsn.fr/en/research/theses-post-docs/theses/defended-thesis/psn-res/pages/2018-scheiff-study-transient-boiling-context-ria-accident-videos.aspx

Declaration of Competing Interest

The authors declare that they have no known competing financial interests or personal relationships that could have appeared to influence the work reported in this paper.

CRediT authorship contribution statement

V. Scheiff: Methodology, Investigation, Formal analysis, Visualization, Writing - original draft. **F. Bergame:** Software, Writing - original draft. **J. Sebilleau:** Conceptualization, Resources, Supervision, Writing - review & editing. **P. Ruyer:** Conceptualization, Supervision, Writing - review & editing. **C. Colin:** Conceptualization, Resources, Supervision, Project administration, Writing - review & editing.

Acknowledgments

This work is funded by Institut de Radioprotection et de Sûreté Nucléaire (IRSN) and Électricité de France (EDF) in the frame of their collaborative research programs. The authors would like to thank Gregory Ehses and Sebastien Cazin from the Institut de Mécanique des Fluides de Toulouse for their technical support on the experimental part including visualisations with high-speed and IR cameras.

Appendix A. Power control

This appendix presents the technical properties of the temperature and power control, performed by using a control loop mechanism : Proportional Integral Derivative.

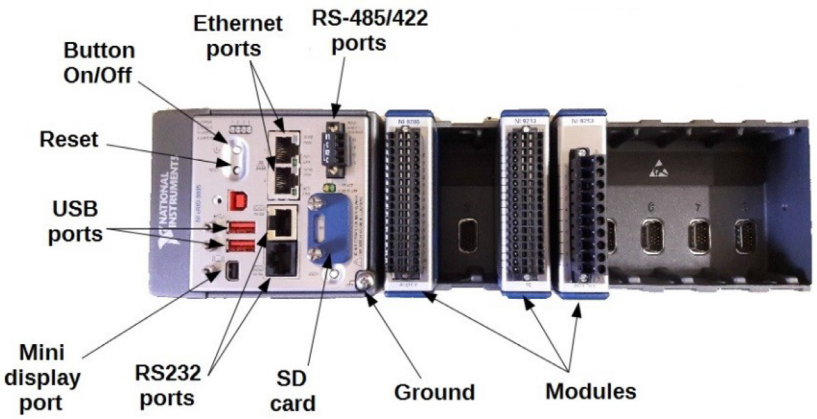

Fig. A1. Compact RIO 9035 with three modules uses by our application.

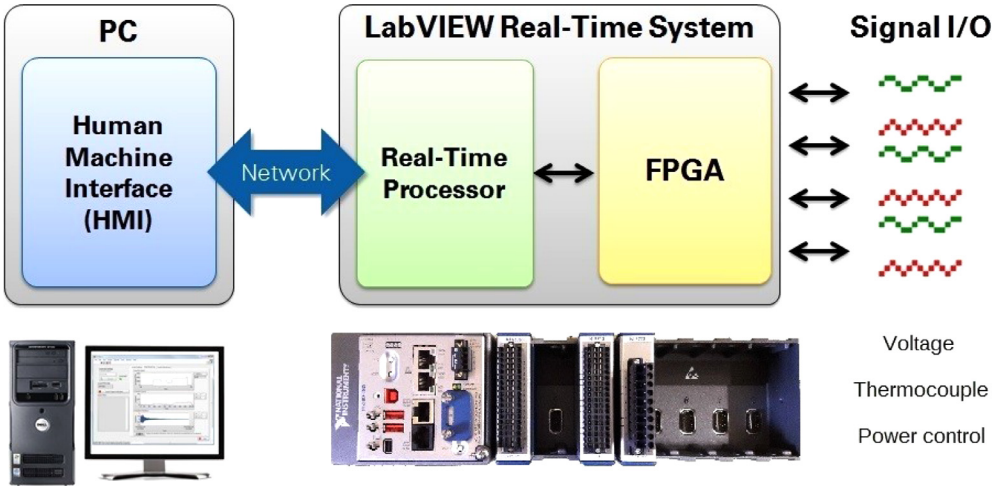

Fig. A2. NI Embedded Control and Monitoring System for our application.

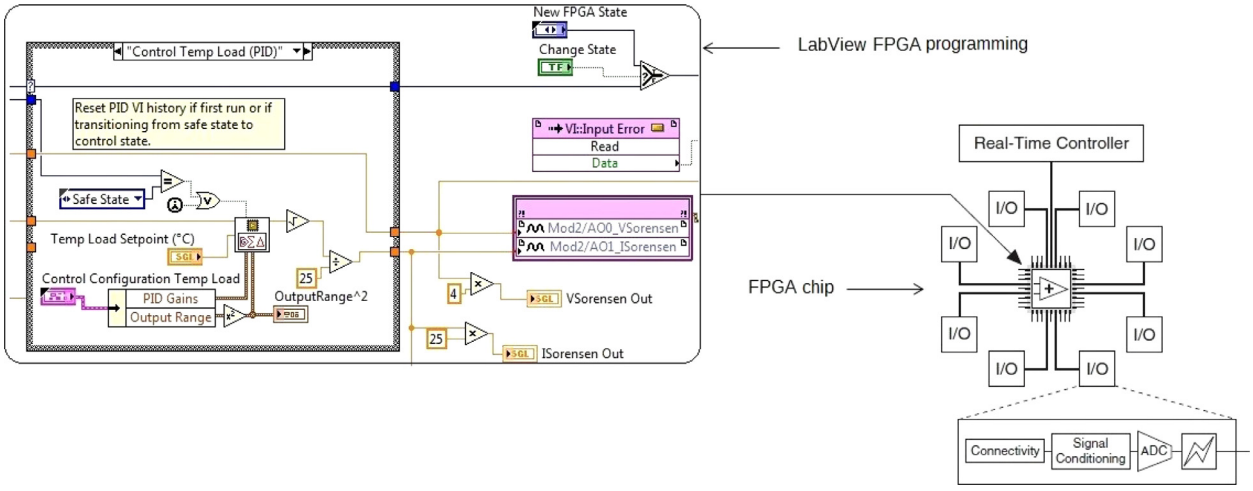

Fig. A3. LabView FPGA programming reconfigure a single FPGA chip.

The device used to control the system is a CompactRIO 9035 which is an embedded controller with different integrate modules developed by National Instruments (Fig. A1).

The CompactRIO 9035 works with Linux real time processor and uses the technology reconfigurable FPGA (Field Programmable Gate Array) to acquire signals and control devices. The CompactRIO 9035 discusses with the Human Machine Interface by the local network via Ethernet port (Fig. A2).

FPGA technology increases the performance of the software program. The FPGA circuitry is a chip that offers the same capacity as an electronic card (instantaneous signals processing). With LabView FPGA programming, the system enables the deployment of an executable file on the CompactRIO device that reconfigure millions logic gates inside a single FPGA chip (Fig. A3).

For comparison, the time response of a DAC system is 25 ms while the time response of a RIO system is 25 ns. In addition, the P.I.D. control loop of RIO system can reach a rate of 200 MHz and simultaneously perform data processing. Thus, with the CompactRIO 9035, we have designed a P.I.D. control for high performance in terms of rapidity, stability and accuracy. In this study, the ramp control is executed at 1000 Sample/s. The signals are acquired at 1000 Hz and the rate of P.I.D. control loop is 200 MHz. These characteristics are largely sufficient to generate temperature ramp with very fast transients ($\geq$ 100K.s^{-1}).

Appendix B. Thermophysical properties

Table B1

Table B1
Thermophysical properties of different materials.

	Foil properties at 20 °C (stainless steel AISI 304)		
Solid	ρ_w (kg.m^{-3})	$C_{p,w}$ (J.kg^{-1}.K^{-1})	λ_w (W.m^{-1}.K^{-1})
	7930	500	16.18
	α_w (m^2.s^{-1})	E_w (J.K^{-1}.m^{-2}.s$^{-1/2}$)	e_w (µm)
	4.08×10^{-6}	8010	50
	Paint properties at 20 °C		
Solid	ρ_p (kg.m^{-3})	$C_{p,p}$ (J.kg^{-1}.K^{-1})	λ_p (W.m^{-1}.K^{-1})
	1200	1480	0.13
	α_p (m^2.s^{-1})	E_p (J.K^{-1}.m^{-2}.s$^{-1/2}$)	e_p (µm)
	7.3×10^{-8}	480	25 – 30
	HFE7000 properties at T_{sat}=35 °C and at P=1 bar		
Fluid	ρ_l (kg.m^{-3})	$C_{p,l}$ (J.kg^{-1}.K^{-1})	λ_l (W.m^{-1}.K^{-1})
	1376	1185	0.073
	α_l (m^2.s^{-1})	ν_l (m^2.s^{-1})	h_{lv} (kJ.kg^{-1})
	4.5×10^{-8}	2.8×10^{-7}	132
	ρ_v (kg.m^{-3})	σ (N.m^{-1})	
	7.9	4.7×10^{-3}	

References

[1] P. Shi, P. Rzehak, D. Lucas, J. Magnaudet, Hydrodynamic forces on a clean spherical bubble translating in a wall-bounded linear shear flow, Phys. Rev. Fluids 5 (2020) 073601.

[2] H. Auracher, W. Marquardt, Heat transfer characteristics and mechanisms along entire boiling curves under steady-state and transient conditions, Int. J. Heat Fluid Flow 25 (2) (2004) 223–242.

[3] A. Sakurai, M. Shiotsu, Transient pool boiling heat transfer-part 2: boiling heat transfer and burnout, J. Heat Transfer 99 (4) (1977) 554–560.

[4] S. Fau, W. Bergez, C. Colin, Transition between nucleate and film boiling in rapid transient heating, Exp. Therm Fluid Sci. 83 (2017) 118–128.

[5] G.-Y. Su, M. Bucci, T. McKrell, J. Buongiorno, Transient boiling of water under exponentially escalating heat inputs. part II: flow boiling, Int. J. Heat Mass Transf. 96 (2016) 685–698.

[6] V. Bessiron, T. Sugiyama, T. Fuketa, Clad-to-coolant heat transfer in NSRR experiments, Journal of Nuclear Science and Technologyy 44 (5) (2007) 723–732.

[7] V. Bessiron, Modelling of clad-to-Coolant heat transfer for RIA applications, J. Nucl. Sci. Technol. 44 (2) (2007) 211–221.

[8] R. Visentini, C. Colin, P. Ruyer, Experimental investigation of heat transfer in transient boiling, Exp. Therm Fluid Sci. 55 (2014) 95–105.

[9] N. Baudin, C. Colin, P. Ruyer, J. Sebilleau, Turbulent flow and transient convection in a semi-annular duct, Int. J. Therm. Sci. 108 (2016) 40–51.

[10] V. Scheiff, N. Baudin, P. Ruyer, J. Sebilleau, C. Colin, Transient flow boiling in a semi-annular duct: from the onset of nucleate boiling to the fully developed nucleate boiling, Int. J. Heat Mass Transf. 138 (2019) 699–712.

[11] I. Golobič, M. Zupančič, Wall-temperature distributions of nucleate pool boiling surfaces vs. boiling curves: a new approach, Int. J. Heat Mass Transf. 99 (2016) 541–547.

[12] J. Petkovsek, Y. Heng, M. Zupancic, H. Gjerkes, F. Cimerman, I. Golobič, Ir thermographic investigation of nucleate pool boiling at high heat flux, Int. J. Refrig 61 (2016) 127–139.

[13] A. Richenderfer, A. Kossolapov, J. Seong, G. Saccone, E. Demarly, R. Kommajosyula, E. Baglietto, B. J., M. Bucci, Investigation of subcooled flow boiling and CHF using high-resolution diagnostics, Exp. Therm Fluid Sci. 99 (2018) 35–58.

[14] M. Kaneda, B. Yu, H. Ozoe, S.W. Churchill, The characteristics of turbulent flow and convection in concentric circular annuli. part i: flow, Int. J. Heat Mass Transf. 46 (26) (2003) 5045–5057.

[15] V. Scheiff, Étude expérimentale et modélisation du transfert de chaleur de l'Ębullition transitoire, Université de Toulouse, 2018 Ph.D. thesis.

[16] J. Chen, Correlation for boiling heat transfer to saturated fluids in convective flow, Industrial & Engineering Chemistry Process Design and Development 5 (3) (1966) 322–329.

[17] F. Dittus, L. Boelter, Heat transfer in automobile radiators of the tubular type, Publication on Engineering 2 (13) (1930) 443.

[18] H. Forster, N. Zuber, Dynamics of vapor bubbles and boiling heat transfer, AIChE J. 1 (4) (1955) 531–535.

[19] D. Butterworth, The correlation of cross flowpressure drop data by means of a permeability concept, Technical Report, AERE-R9435, UKAEA, 1979.

[20] J.G. Collier, J.R. Thome, Convective boiling and condensation, 3rd, Oxford: Clarendon Press, 1994.

[21] N. Baudin, Étude expérimentale et modélisation de l'Ębullition transitoire, Université de Toulouse, 2015 Ph.D. thesis.

[22] O. Zeitoun, M. Shoukri, Bubble behavior and mean diameter in subcooled flow boiling, J. Heat Transfer. 118 (1) (1996) 110–116.

[23] R. Mei, J. Klausner, Unsteady force on a spherical bubble at finite reynolds number with small fluctuations in the free-stream velocity, Physics of Fluids A: Fluid Dynamics (1989–1993) (1992) 63–70.

[24] N. Basu, G.R. Warrier, V.K. Dhir, Wall heat flux partitioning during subcooled flow boiling: part 1model development, J. Heat Transfer. 127 (2) (2005) 131–140.